

# Waves and Instabilities for Model Tropical Convective Parameterizations

ANDREW J. MAJDA AND MICHAEL G. SHEFTER

*Courant Institute of Mathematical Sciences, New York University, New York, New York*

(Manuscript received 22 October 1999, in final form 25 July 2000)

## ABSTRACT

Models of the tropical atmosphere with crude vertical resolution are important as intermediate models for understanding convectively coupled wave hierarchies and also as simplified models for studying various strategies for parameterizing convection and convectively coupled waves. Simplified models are utilized in a detailed analytical study of the waves and instabilities for model convective parameterizations. Three convection schemes are analyzed: a strict quasi-equilibrium (QE) scheme and two schemes that attempt to model the departures from quasi equilibrium by including the shorter timescale effects of penetrative convection, the Lagrangian parcel adjustment (LPA) scheme and a new instantaneous convective available potential energy (CAPE) adjustment (ICAPE) scheme. Unlike the QE parameterization scheme, both the LPA and ICAPE schemes have scale-selective finite bands of unstable wavelengths centered around typical cluster and supercluster scales with virtually identical growth rates and wave structure. However, the LPA scheme has, in addition, two nonphysical superfast parasitic waves that are artifacts of this parameterization while such waves are completely absent in the new ICAPE parameterization.

Another topic studied here is the fashion in which an imposed barotropic mean wind triggers a transition to instability in the Tropics through suitable convectively coupled waves; this is the simplest analytical problem for studying the influence of midlatitudes on convectively coupled waves. For an easterly barotropic mean flow with the effect of rotation included, both supercluster-scale moist Kelvin waves and cluster-scale moist mixed Rossby-gravity waves participate in the transition to instability. The wave and stability properties of the ICAPE parameterization with rotation are studied through a novel procedure involving complete zonal resolution but low-order meridional truncation. Besides moist Kelvin, mixed Rossby-gravity, and equatorial Rossby waves, this approximation retains other slowly propagating moist gravity waves in a consistent fashion.

## 1. Introduction

Important observational features of tropical meteorology, which exhibit a hierarchy of scales as well as waves coupled to moist convection, include faster propagating cloud clusters and superclusters (Nakazawa 1988, and references therein) on scales of order 2000–3000 km within larger-scale slower propagating Madden-Julian waves (Madden and Julian 1972, 1994). The capability of current convective parameterization schemes in general circulation models to represent significant features of this convectively coupled wave hierarchy is an important practical topic (Chao and Lin 1994; Chao and Deng 1998, and references therein).

Theoretical efforts in understanding convectively coupled tropical waves have focused on models with crude vertical resolution involving a dominant baroclinic heating mode coupled to convection (Emanuel 1987; Neelin et al. 1987; Goswami and Goswami 1991;

Yano and Emanuel 1991; Neelin and Yu 1994). Such models of the tropical atmosphere with crude vertical resolution are important as simplified intermediate climate models (Neelin and Zeng 1999, manuscript submitted to *J. Atmos. Sci.*; Zeng and Neelin 1999; Lin et al. 2000) as well as for providing simplified models to study the convectively coupled wave hierarchy through numerical experiments (Yano et al. 1995, hereafter referred to as YM<sup>2</sup>E). These models also provide a simplified analytical context to study various strategies for parameterizing convection (Yano et al. 1998, hereafter referred to as YM<sup>2</sup>).

In this paper, such simplified models with crude vertical resolution are utilized in a detailed analytical study of the waves and instabilities for model convective parameterizations. The convection schemes that are analyzed here attempt to incorporate departures from strict quasi equilibrium (QE) (Arakawa and Schubert 1974; Emanuel 1994) by including the shorter-timescale effects of the mass flux by deep penetrative convection over small areas on the convectively coupled dynamics. The most complicated scheme of this type that is considered here is the Lagrangian parcel adjustment (LPA) scheme introduced in YM<sup>2</sup>E and YM<sup>2</sup> where in a La-

---

*Corresponding author address:* Prof. Andrew J. Majda, Courant Institute of Mathematical Sciences, New York University, 251 Mercer Street, New York, NY 10012.  
E-mail: jonjon@cims.nyu.edu

grangian formulation, vertical motion is generated by convective available potential energy (CAPE). A second new parameterization, which involves instantaneous release of CAPE (the ICAPE scheme), is also introduced. The simplified model with crude vertical resolution and these two convective parameterizations together with a strict QE scheme are developed in section 2. A novel feature is the use of a turbulent boundary layer drag parameterization that allows for the effects of turbulent fluctuations even when the mean flow vanishes (Neelin and Zeng 1999, manuscript submitted to *J. Atmos. Sci.*). This feature allows for a meaningful stable radiative–convective equilibrium without a horizontal mean flow and is important for the studies of transition to instability in subsequent sections of the paper. There is no doubt that convectively coupled tropical waves exhibit both linear and highly nonlinear features. There is some evidence that the strongest nonlinearities are most important at the smallest scales such as from the remarkable recent observations of Wheeler and Kiladis (1999) for convectively coupled waves. Thus, the convective coupling with large-scale tropical waves might be in a weakly nonlinear regime; under such circumstances, linearized stability analysis is a natural way to begin such studies to gain analytic insight. This is the approach adopted in the present paper.

The detailed linearized wave and stability properties of the LPA, ICAPE, and QE convective parameterization schemes are compared in section 3. Unlike the QE parameterization scheme, both the LPA and ICAPE schemes have scale-selective finite bands of unstable wavelengths centered around typical cluster and supercluster scales with virtually identical growth rates, phase velocities, and wave structure for the unstable moist gravity waves. However, the LPA scheme has, in addition, two nonphysical superfast “parasitic” waves that are artifacts of the parameterization. The new ICAPE parameterization has the additional attractive feature that such parasitic waves are absent and are replaced by a strongly damped mode representing finite adjustment of CAPE perturbations.

Finally, the wave and stability properties of the ICAPE parameterization with rotation are studied in section 4 through a novel procedure involving complete zonal resolution but low-order meridional truncation (see section 4a below). Besides moist Kelvin, mixed Rossby–gravity (MRG), and equatorial Rossby waves, this approximation retains other slowly propagating moist gravity waves in a consistent fashion; this may prove useful for comparison of theory with observational studies (Wheeler and Kiladis 1999). The procedure is intermediate in complexity between the equatorial long-wave approximation (Heckley and Gill 1984; Neelin and Yu 1994) and complete meridional resolution on the equatorial  $\beta$  plane.

Another important topic studied here is the fashion in which an imposed constant barotropic mean wind,  $\bar{u}$ , triggers a transition to instability through suitable con-

vectively coupled waves; in other words, for a fixed turbulent drag parameterization and easterly barotropic flow  $\bar{u}$ , there is a critical easterly flow  $\bar{u}_{cr}$  with stability for  $|\bar{u}| < |\bar{u}_{cr}|$  and instability for  $|\bar{u}| > |\bar{u}_{cr}|$  and  $|\bar{u}| - |\bar{u}_{cr}| \ll 1$ . This is the paradigm for studying the influence of midlatitudes on generating convectively coupled tropical waves. For an easterly barotropic flow with rotation, both supercluster-scale moist Kelvin waves and cluster-scale moist MRG waves participate in the transition to instability.

## 2. The model convective parameterizations

In this section several models for convectively coupled dynamics in the Tropics are presented. These models utilize equivalent descriptions of large-scale dynamics and thermodynamics, but differ in the description of the effects of moist convection and its feedbacks into the large-scale dynamics. The atmosphere is represented by two horizontal layers, each with a homogeneous vertical structure (Yano and Emanuel 1991): 1) a dynamically active troposphere and 2) a dynamically passive thin boundary layer coupled to the ocean surface. The stationary spatial fluctuations in the sea surface temperature (SST) drive exchanges of moist potential energy between the two layers via convective updrafts and precipitation downdrafts that are explicitly coupled to the large-scale dynamics. To model convective processes, various convective parameterizations are used that relate the dynamics of convection explicitly through other variables in the system.

This paper discusses three convective parameterization models, which are presented below. Since equations for the large-scale dynamics and dry thermodynamics, as well as some other features, are essentially the same for all models, the common pieces will be described only for the first scheme, with the focus on the differences that arise due to convective parameterizations alone in the subsequent discussions.

The large-scale dynamics in the middle troposphere for all of these schemes is based on a  $1\frac{1}{2}$ -layer model that, following YM<sup>2</sup>E, involves a baroclinic heating mode of the primitive equations on the equatorial  $\beta$  plane:

$$\frac{D\mathbf{v}_H}{Dt} = \bar{\alpha} \nabla \theta - \frac{C_D}{h} \mathcal{D}(|\mathbf{v}_H|) \mathbf{v}_H - \frac{1}{\tau_D} \mathbf{v}_H - \beta y \mathbf{v}_H^\perp. \quad (2.1)$$

Here,  $\mathbf{v}_H(x, y, t)$  is the horizontal large-scale wind with components  $(u, v)$  that depend on the zonal and meridional spatial variables  $x$  and  $y$ , and time  $t$ . The wind above is driven by the following forces, listed as they appear in the equation: the perturbations of the geopotential, expressed via fluctuations of the dry potential temperature,  $\theta$ ; the turbulent drag from the fluctuations in the boundary layer; the Rayleigh relaxation wind forcing; and the Coriolis effect due to rotation. The symbol  $D/Dt$  denotes the substantial derivative including the mean flow,  $\bar{u}$ . The symbol  $\mathbf{v}_H^\perp$  represents the

TABLE 1. Model parameters.

$C_\theta = 1.2 \times 10^{-3}$ , surface-flux rate by wind
$C_D = 10^{-3}$ , surface heating coefficient
$N = 10^{-2} \text{ s}^{-1}$ , Brunt-Väisälä buoyancy frequency
$\epsilon = (\theta_0 - \theta)/(\theta_0) \sim 0.1$ , strength of temperature fluctuations in the troposphere
$\theta_0 = 300 \text{ K}$ ; temperature at the top of the boundary layer
$\theta_{eb}^* = 10 \text{ K}$ ; size of fluctuations in the boundary layer moist potential temperature
$\epsilon_p = 0.9$ , precipitation efficiency coefficient
$\Gamma_m = 6 \times 10^{-3} \text{ K m}^{-1}$ , moist lapse rate
$\gamma = 1.7$ , ratio of moist and dry lapse rates
$c_p = 10^3 \text{ J K}^{-1} \text{ kg}^{-1}$ , specific heat at constant pressure
$Q_{R0} = -1 \text{ K day}^{-1}$ , mean radiative cooling rate
$\tau_R = 50 \text{ days}$ , longwave radiation relaxation time
$\tau_D = 75 \text{ days}$ , Rayleigh forcing timescale
$H = 8 \text{ km}$ , depth of the troposphere
$H_m = 5 \text{ km}$ , depth of the middle-level troposphere (a level of minimum moist potential temperature)
$h = 500 \text{ m}$ , thickness of subcloud boundary layer

orthogonal vector with components,  $(-v, u)$ . To shorten the notation, the coefficient  $\bar{\alpha} = \gamma \epsilon c_p$  has been introduced. All other constants are described in Table 1. In addition to various forcings, dynamics is also included through the barotropic mean wind,  $\bar{u}$ , which is assumed to be prescribed externally. The representation of all forcing terms except the turbulent drag is conventional; the modeling of turbulent drag will be addressed later.

The total vertical velocity is decomposed into a large-scale environmental circulation, which occurs throughout almost the entire troposphere, and the convective updrafts, which represent the deep penetrative activity in a large number of narrow convective towers. All of these towers are assumed to be identical, with the updraft mean velocity,  $w_c(x, y, t)$ , and overall area that represents a fraction  $\sigma_c$  of the horizontal area of the entire troposphere. Quantitatively, the vertical velocity can be expressed via the speed of compensating environmental descent,  $w_e$ , and convective updrafts,  $w_c$ :

$$w = (1 - \sigma_c)w_e + \sigma_c w_c.$$

Then, conservation of mass assumes the following form:

$$\text{div}_H \mathbf{v}_H + (1 - \sigma_c) \frac{w_e}{H_m} = -\sigma_c \frac{w_c}{H_m}, \quad (2.2)$$

with  $H_m$  the height of the middle troposphere.

Next, it is assumed that fluctuations in the dry potential temperature are driven by warming caused by

the environmental descent,  $w_e$ , which brings down potentially warmer air from the upper layers of the atmosphere to the boundary layer, and also by radiative losses from the top of the troposphere; that is,

$$\frac{D\theta}{Dt} = -\frac{N^2}{g} \theta_0 w_e + Q_R. \quad (2.3)$$

Here, radiative losses are represented by the Newtonian cooling rate,  $Q_R = Q_{R0} - \theta/\tau_R$ , with a constant equilibrium cooling rate,  $Q_{R0} = -1 \text{ K day}^{-1}$ , and radiative damping, with relaxation time,  $\tau_R$ . Combining conservation of mass in (2.2) and the equation in (2.3),  $w_e$  is eliminated to obtain the prognostic equation for the dry potential temperature,  $\theta$ :

$$(1 - \sigma_c) \frac{D\theta}{Dt} - \bar{\alpha} \text{div}_H \mathbf{v}_H = \frac{\bar{\alpha}}{H_m} \sigma_c w_c + Q_R. \quad (2.4)$$

Here, the following coefficient,

$$\bar{\alpha} = \frac{H_m N^2 \theta_0}{g}, \quad (2.5)$$

has been utilized for simplicity in notation. Following YM<sup>2</sup>E, the moist thermodynamic exchanges between the lower troposphere (also referred to as the subcloud boundary layer) and middle troposphere satisfy the equations

$$h \frac{D\theta_{eb}}{Dt} = -D_d + E, \quad H \frac{D\theta_{em}}{Dt} = D_d + HQ_R, \quad (2.6)$$

$$Q_R = Q_{R0} - \frac{\theta}{\tau_R}.$$

In these equations, the term  $E$  represents forcing provided by the latent heat flux from the boundary layer. The losses are represented by radiative cooling of the top of the troposphere, and the two layers communicate through downdrafts  $D_d$ . Following YM<sup>2</sup>E and YM<sup>2</sup>,

$$E = C_\theta \mathcal{D}(|\mathbf{v}_H|)(\theta_{eb}^* - \theta_{eb}),$$

$$D_d = -[(1 - \sigma_c)w_e^\downarrow - \sigma_c w_d](\theta_{eb} - \theta_{em}). \quad (2.7)$$

Here,  $\theta_{eb}$  and  $\theta_{eb}^*$  are the equivalent moist potential temperature and saturated moist potential temperature above the ocean surface;  $\theta_{em}$  is the equivalent moist potential temperature in the middle troposphere;  $w_e^\downarrow = w_e \mathcal{H}(-w_e)$ , where  $\mathcal{H}$  is the Heaviside function; and  $C_\theta \mathcal{D}(|\mathbf{v}_H|)$  is the turbulent heat-flux rate. The precipitation effects are represented implicitly by convective downdrafts,  $w_d$ , which in this simple model are proportional to convective updrafts:

$$w_d = \frac{1 - \epsilon_p}{\epsilon_p} w_c, \quad (2.8)$$

with the precipitation efficiency,  $\epsilon_p$ .

In the analysis below, the equation that describes the dynamics of  $\theta_{em}$  in (2.6) is replaced by an equivalent equation for the potential temperature vertically aver-

aged over the two layers,  $\langle \theta_e \rangle_z \approx h/H\theta_{eb} + \theta_{em}$ , with the following prognostic equation:

$$\frac{D\langle \theta_e \rangle_z}{Dt} = \frac{1}{H}E + Q_R. \quad (2.9)$$

The use of  $\langle \theta_e \rangle_z$  rather than  $\theta_{em}$  is motivated by the fact that without forcing, the vertically integrated moist potential temperature is essentially conserved (Emanuel 1994).

*Modeling of the boundary layer turbulent drag.* Friction exerted by turbulent fluctuations in the boundary layer on the free troposphere is typically modeled with a turbulent drag term. A number of authors (YM<sup>2</sup>E; YM<sup>2</sup>) use the magnitude of horizontal wind,

$$\mathcal{D}(|\mathbf{v}_H|) = |\mathbf{v}_H|, \quad (2.10)$$

to model the drag. However, boundary layer turbulence that drives the friction mechanism occurs even in the absence of large-scale wind. Instead of (2.10), the authors use a more general representation,

$$\mathcal{D}(|\mathbf{v}_H|) = (u_0^2 + |\mathbf{v}_H|^2)^{1/2}, \quad u_0^2 \neq 0, \quad (2.11)$$

also utilized by Neelin and Zeng (1999, manuscript submitted to *J. Atmos. Sci.*). The constant  $u_0$  above represents the typical size of turbulent velocity fluctuations. Neelin and Zeng (1999, manuscript submitted to *J. Atmos. Sci.*) use values for  $u_0$  as large as  $5 \text{ m s}^{-1}$ . It is easy to see that the representation in (2.10) can be recovered from (2.11) by setting  $u_0 = 0$ . The presence of nonzero turbulent fluctuations in (2.11) is useful for the following reasons. First, it permits the system that describes convectively coupled dynamics to have reasonable values at radiative–convective equilibrium without having to impose a large-scale mean flow. Also, by allowing the parameter  $u_0$  to vary, one can study how properties of the system depend on the intensity of turbulent drag. Finally, with the drag in (2.11), the changes in stability properties can be recast very naturally as response of the system to changing barotropic mean wind; all of these points will be addressed later in section 3.

#### a. The Lagrangian parcel adjustment scheme

In order to obtain a closed system for convectively driven large-scale dynamics, it is necessary to use a convective parameterization that defines feedbacks from convective activity to the large-scale dynamics and thermodynamics. The specific form of this relationship determines the models discussed in this paper.

In the LPA scheme, the convective updrafts adjust dynamically to positive feedbacks from the fluctuations of the CAPE and to negative feedbacks from the kinetic energy of convective updrafts. The prognostic equation associated with the LPA scheme, formulated in YM<sup>2</sup>E and YM<sup>2</sup>, has the form

$$\frac{Dw_c}{Dt} = \left( \frac{c_p \Gamma_m}{\theta_0} B - \frac{w_c^2}{2H} \right) \mathcal{H}(w_c). \quad (2.12)$$

In this expression,  $B = \theta_{eb} - \theta_{em}^*$  is the convective buoyancy, where saturated moist potential temperature,  $\theta_{em}^*$ , is related to the dry potential temperature by

$$\theta_{em}^* = \gamma\theta.$$

The term  $(c_p \Gamma_m B)/(\theta_0)$  in (2.12) expresses buoyancy force due to the fluctuations in CAPE, and  $(w_c^2)/(2H)$  stands for kinetic energy of updrafts. The Heaviside factor is utilized here to emphasize that convection can occur only in the positive vertical direction, with warm and moist air evaporating from the ocean surface and rising through the boundary layer.

In the LPA parametrization, the prognostic variables involve the large-scale wind,  $\mathbf{v}_H$ ; the dry potential temperature,  $\theta$ ; the vertical velocity of convective updrafts,  $w_c$ ; the moist equivalent potential temperature in the boundary layer,  $\theta_{eb}$ ; and the averaged moist potential temperature,  $\langle \theta_e \rangle_z$ , or equivalently,  $\theta_{em}$ . Downdrafts, both environmental and convective, are determined diagnostically, using conservation of mass in (2.2) and the relation in (2.8).

#### b. Instantaneous adjustment to CAPE fluctuations

The LPA equation in (2.12) expresses dynamic adjustment of convective updrafts to the variations in CAPE. When CAPE fluctuations are entirely balanced by the kinetic energy of updrafts, the left-hand side of (2.12) vanishes and no dynamics for the small-scale vertical velocity occurs. Thus, in the ICAPE scheme the equation in (2.12) is replaced by the diagnostic relation

$$\frac{w_c^2}{2H} = \frac{c_p \Gamma_m}{\theta_0} (\theta_{eb} - \gamma\theta) \mathcal{H}(\theta_{eb} - \gamma\theta). \quad (2.13)$$

Here, the Heaviside factor is utilized because only positive CAPE fluctuations can drive convective updrafts. Otherwise, all other equations in the ICAPE model are exactly equivalent to their analogs in the LPA scheme.

The effects of precipitation are modeled by the convective downdraft contributions, according to (2.8). An interesting question is how the small-scale convective downdrafts influence stability and other properties in the system compared with the influence of environmental descent on larger scales. As a paradigm the convective part of the downdraft  $D$ , defined in (2.7), is replaced by

$$D^* = -(1 - \sigma_c)w_e^d(\theta_{eb} - \theta_{em}). \quad (2.14)$$

Mathematically, the absence of convective downdrafts is equivalent to setting  $\epsilon_p = 1$  in (2.8). In section 3d the representation above will be utilized to address the influence of small-scale convective downdrafts for the ICAPE system.

### c. Quasi-equilibrium scheme

Following YM<sup>2</sup>E and YM<sup>2</sup>, no buoyancy fluctuations are permitted and  $B = 0$ , based on the original instantaneous statistical QE idea of Arakawa and Schubert (1974). This restriction of zero buoyancy yields that

$$\frac{D(\theta_{eb} - \gamma\theta)}{Dt} \equiv 0. \quad (2.15)$$

By using (2.15) and combining the equations for  $\theta$  and  $\theta_{eb}$ , one easily obtains a nonlinear equation for the intensity of convective updrafts in terms of the large-scale winds and remaining thermodynamic variables:

$$\begin{aligned} & \frac{C_\theta}{h} \mathcal{D}(|\mathbf{v}_H|)(\theta_{eb}^* - \gamma\theta) \mathcal{H}(\theta_{eb}^* - \gamma\theta) \\ & - \left[ \left( \frac{\sigma_c}{h} w_c + \frac{H_m}{h} \text{div}_H \mathbf{v}_H \right) \mathcal{H} \left( \frac{\sigma_c}{h} w_c + \frac{H_m}{h} \text{div}_H \mathbf{v}_H \right) \right. \\ & \quad \left. + \frac{1 - \epsilon_p \sigma_c}{\epsilon_p} \frac{\sigma_c}{h} w_c \right] \times [\gamma\theta(1 + h/H) - \langle \theta_e \rangle_z] \\ & = \frac{\gamma \bar{\alpha} \sigma_c}{H_m} w_c + \gamma \mathcal{Q}_R + \gamma \bar{\alpha} \text{div}_H \mathbf{v}_H. \end{aligned} \quad (2.16)$$

The number of prognostic variables needed to describe the dynamics based on the QE scheme is further decreased, as compared with the LPA and ICAPE schemes. Only the large-scale winds,  $\mathbf{v}_H$ ; the dry potential temperature,  $\theta$ ; and the quantity  $\langle \theta_e \rangle_z$  are obtained prognostically. The moist equivalent potential temperature  $\theta_{eb}$  is determined trivially from the CAPE conservation condition,  $\theta_{eb} = \gamma\theta$ , while  $w_c$  is found from (2.16). Environmental descent and convective downdrafts are related to the other variables through the same diagnostic relations as in the LPA and ICAPE schemes.

### 3. Waves and instabilities for LPA and ICAPE schemes

Section 2 was devoted to the discussion of several models for large-scale dynamics in the Tropics coupled with convective activity based on three convective parameterizations. The parameters used are reported in Table 1 without further explanation and are identical to those utilized in YM<sup>2</sup>E and YM<sup>2</sup>, which the reader can consult for detailed motivation. For example, the time-scale of Rayleigh forcing has been set at 75 days in YM<sup>2</sup>E to give plausible physical results in the numerical simulations and similar values to those utilized in other idealized studies. In the following sections the properties of the linearized equations that describe small departures from a radiative–convective equilibrium state based on these convective parameterizations are detailed. The specific features of convective parameterizations can alter significantly the behavior at small scales and LPA specifically introduces physically irrelevant parasitic modes. It is demonstrated that the pa-

rameterization introduced in section 2 based on the ICAPE mechanism is free of many of the defects associated with the other parameterizations.

#### a. Radiative–convective equilibrium and the linear system

In radiative–convective equilibrium (RCE), forcing generated by fluctuations in the SST is exactly balanced by radiative cooling from the top of the troposphere through time-independent convective updrafts and downdrafts. Since  $\sigma_c$  is typically a small number, the approximation  $(1 - \sigma_c) \approx 1$  in (2.4) will be henceforth used for simplicity. The following radiative–convective equilibrium conditions, valid for both the LPA and ICAPE schemes, are

$$\begin{aligned} & \frac{\bar{\alpha} \sigma_c}{H_m} \bar{w}_c + \mathcal{Q}_{R0} = 0, \\ & (\bar{\theta}_{eb} - \gamma \bar{\theta}) = \frac{\bar{w}_c^2 \theta_0}{2c_p \Gamma_m H}, \\ & \frac{C_\theta}{h} (u_0^2 + \bar{u}^2)^{1/2} (\theta_{eb}^* - \bar{\theta}_{eb}) = \frac{1}{h} \left( \frac{\sigma_c \bar{w}_c}{\epsilon_p} \right) \\ & \quad \times \left[ \bar{\theta}_{eb} \left( 1 + \frac{h}{H} \right) - \langle \bar{\theta}_e \rangle_z \right], \\ & \frac{C_\theta}{H} (u_0^2 + \bar{u}^2)^{1/2} (\theta_{eb}^* - \bar{\theta}_{eb}) = -\mathcal{Q}_{R0}. \end{aligned} \quad (3.1)$$

The relations above define equilibrium variables denoted by bars. The remaining variables, such as  $\bar{w}_c$  and  $\bar{w}_d$ , can be recovered by using diagnostic relations (2.2) and (2.8). A key point is that with the turbulent drag in (2.11), an RCE state can be defined in a meaningful way even if the barotropic mean wind is zero.

An RCE state is listed below, where turbulent fluctuations are fixed at  $u_0 = 2 \text{ m s}^{-1}$ , and with barotropic mean wind,  $\bar{u} = -2 \text{ m s}^{-1}$ . The particular values at the equilibrium can vary slightly with these two parameters, but qualitative trends remain valid for a wide range of  $u_0$  and  $\bar{u}$ . In particular, the stability and wave properties established in the remaining parts of the paper are qualitatively correct for perturbations around other realistic RCE states. The parameter choices here are selected to coincide with the RCE state in YM<sup>2</sup>E and YM<sup>2</sup> so that a direct comparison can be made.

- 1) The velocity associated with mean cumulus updrafts,  $\bar{w}_c = -(Q_{R0} H_m) / (\bar{\alpha} \sigma_c)$ , is inversely proportional to the area fraction,  $\sigma_c$ . For  $\sigma_c = 0.01$  it is easy to compute that  $\bar{w}_c \approx 0.4 \text{ m s}^{-1}$ , while for a smaller area fraction,  $\sigma_c = 0.002$ , the corresponding value is,  $\bar{w}_c \approx 2 \text{ m s}^{-1}$ .
- 2) Mean environmental subsidence is determined from the zero–total vertical velocity condition,  $w = 0$ , and is equal to

$$\bar{w}_c = \frac{-\sigma_c \bar{w}_c}{1 - \sigma_c} \approx -0.004 \text{ m s}^{-1}.$$

It is clear that environmental subsidence is essentially independent of  $\sigma_c$ , at least for small values of  $\sigma_c$ .

- 3) For mean moist potential temperature fluctuations in the middle troposphere and in the boundary layer the following estimates are valid:

$$(\theta_{eb}^* - \bar{\theta}_{eb}) = -\frac{HQ_{R0}}{C_\theta(u_0^2 + \bar{u}^2)^{1/2}} \approx 27 \text{ K},$$

$$\left[ \bar{\theta}_{eb} \left( 1 + \frac{h}{H} \right) - \langle \bar{\theta}_e \rangle_z \right] = -\frac{\epsilon_p HQ_{R0}}{\sigma_c \bar{w}_c} \approx 21 \text{ K}.$$

- 4) Mean fluctuations of  $\theta_{eb} - \gamma\theta$ , which define CAPE at the RCE state, are equal to

$$\begin{aligned} (\bar{\theta}_{eb} - \gamma\bar{\theta}) &= \frac{\bar{w}_c^2 \theta_0}{2c_p \Gamma_m H} \\ &\approx \begin{cases} 0.0004 \text{ K}, & \text{for } \sigma_c = 0.01 \\ 0.01 \text{ K}, & \text{for } \sigma_c = 0.002. \end{cases} \end{aligned}$$

The comparison of  $(\bar{\theta}_{eb} - \gamma\bar{\theta})$  with other equilibrium values shows that CAPE fluctuations at equilibrium are indeed much weaker than other potential temperature fluctuations in the system (Emanuel et al. 1994). This is often used to justify the use of a quasi-equilibrium convective parameterization that prohibits any CAPE fluctuations:

$$\bar{\theta}_{eb} - \gamma\bar{\theta} = 0.$$

This relation constitutes the only (small) difference be-

tween radiative-convective equilibrium for the QE scheme and the two other schemes.

Henceforth it will be convenient to use nondimensional variables that are naturally set by the RCE state. In particular, the following velocity scale for large-scale dynamics is utilized,  $V = (\bar{\alpha}\alpha)^{1/2} \approx 50 \text{ m s}^{-1}$ , which coincides with the propagation speed of dry Kelvin wave. The equatorial Rossby radius sets the length scale,  $L = 1500 \text{ km}$ . These scales yield the timescale,  $T = L/V \approx 1/3 \text{ day}$ . Note that with this choice of scales the equatorial parameter  $\beta$  has a unit nondimensional size. A natural scale for temperature fluctuations is given by the moist saturated equivalent potential temperature in the boundary layer,  $\theta_{eb}^*$ . Finally, the value of equilibrium convective updrafts,

$$W = -\frac{Q_{R0} H_m}{\bar{\alpha} \sigma_c}, \quad (3.2)$$

sets the scale for fluctuations in  $w_c$ .

The linearization procedure for the three parameterizations, LPA, ICAPE, and QE, about the RCE is straightforward. The resulting linear systems for all three parameterizations are reported below in the nondimensional units described earlier. In these equations, advection by the barotropic mean wind has been removed by using a standard Galilean shift,  $x' = x - \bar{u}t$ . Here in section 3, the effects of rotation are also neglected by assuming a quasi-one-dimensional structure in the zonal direction for all the variables, or equivalently, by ignoring  $y$  variations. Under these assumptions the linearized equations around the RCE state become

$$\begin{aligned} \frac{\partial u'}{\partial t} &= -\frac{C_D L}{h} \frac{2\bar{u}^2 + u_0^2}{(\bar{u}^2 + u_0^2)^{1/2}} u' + \frac{\bar{\alpha} \theta_{eb}^*}{V^2} \frac{\partial \theta'}{\partial x'} - \frac{T}{\tau_D} u' & \frac{\partial \theta'}{\partial t} &= \frac{\bar{\alpha}}{\theta_{eb}^*} \frac{\partial u'}{\partial x'} - \frac{T}{\tau_R} \theta' + \frac{T |Q_{R0}|}{\theta_{eb}^*} w'_c \\ \frac{\partial \langle \theta'_e \rangle_z}{\partial t} &= \frac{C_\theta L}{h} \frac{h}{H} \left[ (1 - \bar{\theta}_{eb}) \frac{\bar{u}}{(\bar{u}^2 + u_0^2)^{1/2}} u' - (\bar{u}^2 + u_0^2)^{1/2} \theta'_{eb} \right] - \frac{T}{\tau_R} \theta' \\ \frac{\partial \theta'_{eb}}{\partial t} &= \frac{C_\theta L}{h} \left[ (1 - \bar{\theta}_{eb}) \frac{\bar{u}}{(\bar{u}^2 + u_0^2)^{1/2}} u' - (\bar{u}^2 + u_0^2)^{1/2} \theta'_{eb} \right] - \left( \frac{TW\sigma_c}{h\epsilon_p} w'_c + \frac{H_m}{h} \frac{\partial u'}{\partial x'} \right) \left[ \bar{\theta}_{eb} \left( 1 + \frac{h}{H} \right) - \langle \bar{\theta}_e \rangle_z \right] \\ &\quad - \frac{TW\sigma_c}{h\epsilon_p} \left[ \theta'_{eb} \left( 1 + \frac{h}{H} \right) - \langle \theta'_e \rangle_z \right], & & \text{not needed for QE} \\ w'_c &= \frac{c_p \Gamma_m H}{W^2} \frac{\theta_{eb}^*}{\theta_0} (\theta'_{eb} - \gamma\theta'), & & \text{used in ICAPE} \\ \frac{\partial w'_c}{\partial t} &= \frac{c_p \Gamma_m T}{W} \frac{\theta_{eb}^*}{\theta_0} (\theta'_{eb} - \gamma\theta') - \frac{TW}{H} w'_c, & & \text{used in LPA} \\ \theta'_{eb} &= \gamma\theta', \quad w'_c = L_1 u - L_2 \frac{\partial u'}{\partial x'} - L_3 \theta' + L_4 \langle \theta'_e \rangle_z, & & \text{used in QE,} \end{aligned} \quad (3.3)$$

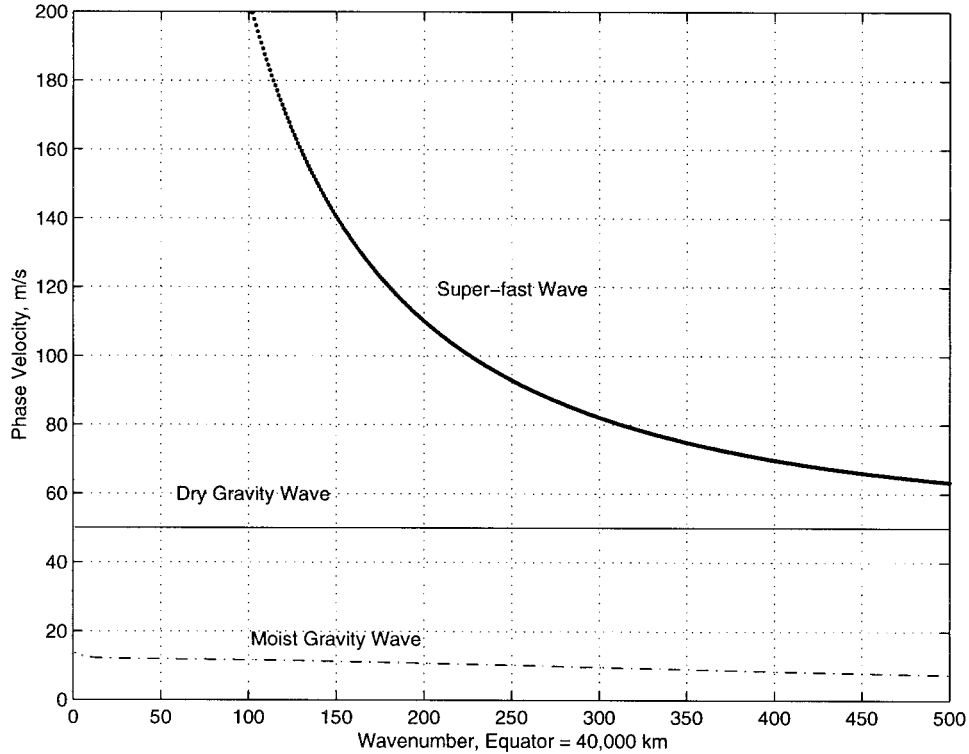


FIG. 1. Phase velocity diagram for moist eastward superfast waves (thick solid line) and moist eastward gravity waves (dash-dotted line) in the LPA system without rotation. The speed of dry gravity waves is indicated by a thin solid line.

with the constants

$$L_1 = \frac{C_\theta L}{h} (1 - \bar{\theta}_{eb}) \frac{\bar{u}}{(u_0^2 + \bar{u}^2)^{1/2}} K^{-1},$$

$$L_2 = \left[ \frac{H_m}{h} + \frac{\gamma \bar{\alpha}}{\theta_{eb}^*} \right] K^{-1},$$

$$L_3 = \left[ \frac{C_\theta L \gamma}{h} (u_0^2 + \bar{u}^2)^{1/2} + \frac{TW\sigma_c}{h\epsilon_p} \gamma \left( 1 + \frac{h}{H} \right) - \gamma \frac{T}{\tau_R} \right] K^{-1},$$

$$L_4 = \frac{TW\sigma_c}{h\epsilon_p} K^{-1},$$

$$K = \frac{TW\sigma_c}{h\epsilon_p} \left[ \bar{\theta}_{eb} \left( 1 + \frac{h}{H} \right) - \langle \bar{\theta}_e \rangle_z \right] + \frac{\gamma T Q_{R0}}{\theta_{eb}^*}.$$

For simplicity, the primes in linearized equations will be discarded throughout the rest of this section. It is easy to verify that large-scale horizontal wind and dry temperature in the equations in (3.3) evolve according to the linear damped shallow-water equations, coupled with moist thermodynamic processes through the convective updrafts, in the last term of the second equation in (3.3).

In the following sections various properties of linear eigenmodes in the form,  $\mathbf{U} = \mathbf{C}e^{i(kx - \omega(k)t) + d(k)t}$ , will be

discussed and compared for the linearized systems that arise for several convective parameterizations considered in this paper. In this analysis, for each wavenumber,  $k$  (or wavelength,  $40\,000/k$  km), real and imaginary parts of a corresponding eigenvalue are treated separately using the following terminology. The properly scaled real part,  $d(k)$ , is naturally called the growth rate, while the imaginary part,  $\omega(k)$ , is referred to as the phase. The scaled ratio  $\omega(k)/k$  and derivative  $d\omega(k)/dk$  are called the generalized phase velocity (GPhV) and generalized group velocity (GGrV). Naturally, GPhV and GGrV coincide with regular phase and group velocity only if the underlying eigenvalue is purely imaginary and has no growth associated with it.

*b. Waves in the LPA system*

The system of linearized equations for LPA in (3.3) involves five prognostic equations and, therefore, at each wavenumber it has five complex eigenvalues. The meaning of all five branches of eigenvalues will be illustrated for the standard set of physical constants from Table 1, along with easterly mean wind,  $\bar{u} = -2$  m s<sup>-1</sup>, and turbulent velocity fluctuations with intensity,  $u_0 = 2$  m s<sup>-1</sup>. Figure 1 presents the GPhV diagram for this case. Since the GPhV diagram is essentially symmetric about  $\omega(k) = 0$ , it suffices to present only its upper part,

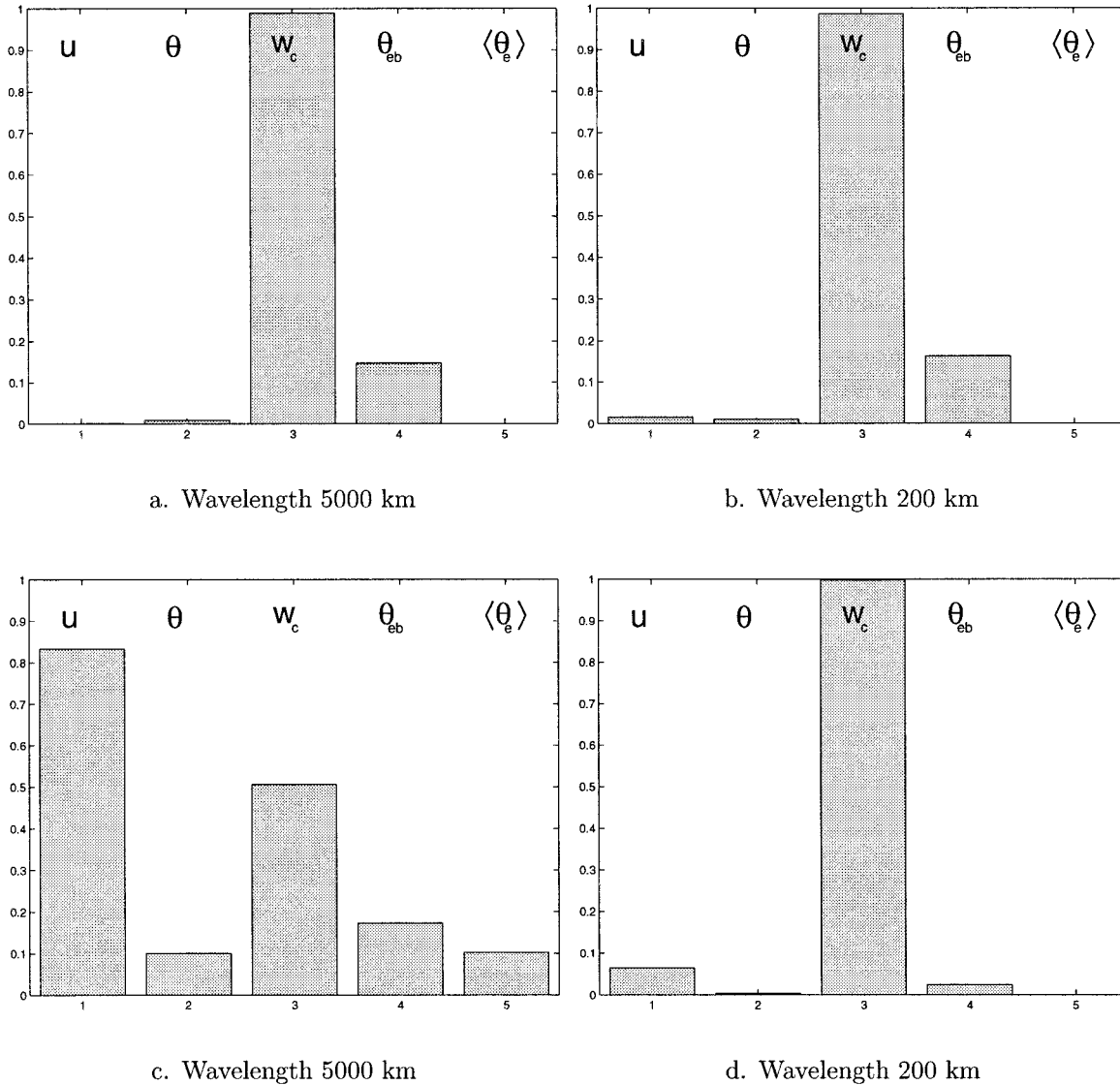


FIG. 2. Eigenvector structure of moist eastward superfast waves, (a) and (b), and moist eastward gravity waves, (c) and (d), for the LPA system without rotation. The wavelengths are 5000 km for (a) and (c), and 200 km for (b) and (d).

where  $\omega(k)/k > 0$ . Among the five branches, there are two eastward waves, shown in Fig. 1, with  $\omega(k) > 0$ , two westward waves with  $\omega(k) < 0$ , and one wave that is essentially standing, with  $\omega(k) \approx 0$ , for all wavenumbers  $k$ .

In order to give a physical interpretation of the various waves, it is important to analyze the eigenvector structure corresponding to each of the eigenvalues. An economical and illustrative way of representing eigenvector structure is given by using bar diagrams (such as depicted in Figs. 2 and 4). Here, each of the variables is represented by a single bar on a diagram, weighted according to the magnitude of the corresponding (typically complex valued) nondimensional component of the eigenvector. Each magnitude is then multiplied by its appropriate dimensional scale, and the overall set of bars

is normalized so that it has a total unit weight. Such a representation allows one to compare relative intensities of various components in an eigenmode.

For the LPA scheme, one pair of eastward and westward propagating waves is significantly faster than the second pair of propagating waves, for all wavenumbers reported in Fig. 1. For example, the generalized phase velocity of the slower pair of waves at a supercluster scale,  $L = 2000$  km, is approximately  $12 \text{ m s}^{-1}$ , while the faster waves with the same wavenumber propagate with an enormous GPhV of approximately  $700 \text{ m s}^{-1}$ . Note that the generalized phase velocity of the fast waves is large even at the small scales, with the smallest value of  $50 \text{ m s}^{-1}$ , which is achieved in the limit of large  $k$ . The speed of dry gravity wave,  $50 \text{ m s}^{-1}$ , is also shown in this figure as a benchmark.

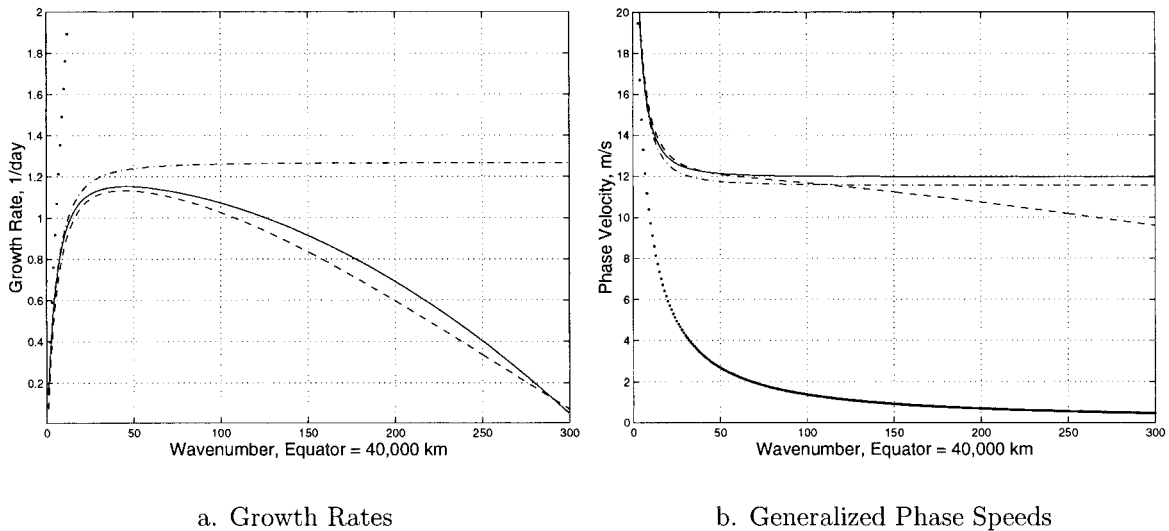


FIG. 3. Linear properties for unstable modes: (a) the growth rates ( $\text{day}^{-1}$ ) and (b) generalized phase velocities ( $\text{m s}^{-1}$ ) for dynamics at the equator with the following convective parameterizations: ICAPE (solid line), LPA (long-dashed line), QE (dot-dashed line), and ICAPE without convective downdrafts (dotted line).

The bar diagrams in Figs. 2a,b show that the faster modes are essentially dominated by small-scale convective gusts, expressed by the variable  $w_c$ , coupled to variations in the boundary layer equivalent potential temperature,  $\theta_{eb}$ , in a wide range of scales, illustrated with a relatively large scale,  $L = 5000$  km, and a smaller scale of  $L = 200$  km. On the other hand, the slower waves, illustrated in Figs. 2c,d, carry strong fluctuations of the large-scale wind,  $u$ , coupled with the dry potential temperature fluctuations through a mechanism similar to dry gravity waves. Convective coupling of these waves, reflected by the large amplitudes of fluctuations in  $w_c$ ,  $\theta_{eb}$ , and  $\langle \theta_e \rangle_z$  in Figs. 2c,d, causes a significant decrease in phase velocity from  $50 \text{ m s}^{-1}$ , the value for dry gravity waves, to approximately  $12 \text{ m s}^{-1}$ . These points indicate that one may identify the slower pair of waves as the eastward and westward moist gravity waves, while the faster pair of waves can be called the superfast waves, motivated by their extremely large phase velocities. The remaining standing wave corresponds to the almost conservation of  $\langle \theta_e \rangle_z$  discussed at the beginning of section 2, and is dominated by the fluctuations of  $\langle \theta_e \rangle_z$ ; this wave will be referred to as the  $\langle \theta_e \rangle_z$  mode.

It is worthwhile to analyze the full physical picture associated with eigenvectors of (3.3) for all waves involved in this system. The intensity of updraft convective activity in the ICAPE parametrization is diagnostically linked to the large-scale flow (which is entirely two-dimensional in the zonal and vertical directions) and, therefore, must be in phase with the ascending branch of the large-scale circulation. This effect is indeed observed for moist gravity waves and the  $\langle \theta_e \rangle_z$  mode (not graphed here due to the space limitations). For the superfast waves, though, the opposite occurs,

where convective updrafts are out of phase with the ascending branch of the large-scale circulation. This fact, along with the superfast phase velocities and the eigenstructure from Figs. 2a,b dominated by vertical gusts, demonstrates that the superfast modes are, in fact, nonphysical parasitic waves, generated as artifacts of the LPA convective parameterization.

Up to this point the discussion involved only the wave properties of normal modes based on the imaginary parts of eigenvalues. On the other side, the stability properties, associated with growth rates, select the modes that will most probably play an important role in the fully nonlinear regime of dynamics. For the current example it is observed that in response to easterly mean wind, the eastward moist gravity wave (the slower eastward branch in Fig. 1) has instability in the wide range of wavelengths,  $150 \text{ km} < L < 20\,000 \text{ km}$ . The peak of instability is located near  $L = 1000$  km, with the maximum growth rate of approximately  $1.2 \text{ day}^{-1}$ . The growth rate diagram is represented by a long-dashed curve in Fig. 3a. All other modes in this example are damped at all wavenumbers with various damping rates, except for the  $\langle \theta_e \rangle_z$  mode, which is essentially neutral. Clearly, due to the absence of rotation or any other symmetry-breaking effects apart from the direction of mean wind in (3.3), west and east are entirely equivalent here. Therefore, the response to westerly mean wind is exactly symmetric, with the same instability of a westward moist gravity wave instead of an eastward moist gravity wave. Following common practice, easterly mean winds will be given a preference here since they naturally mimic circulation associated with a Walker cell observed in the Pacific.

Finally, it is important to point out that the superfast waves can themselves create weak linear instabilities.

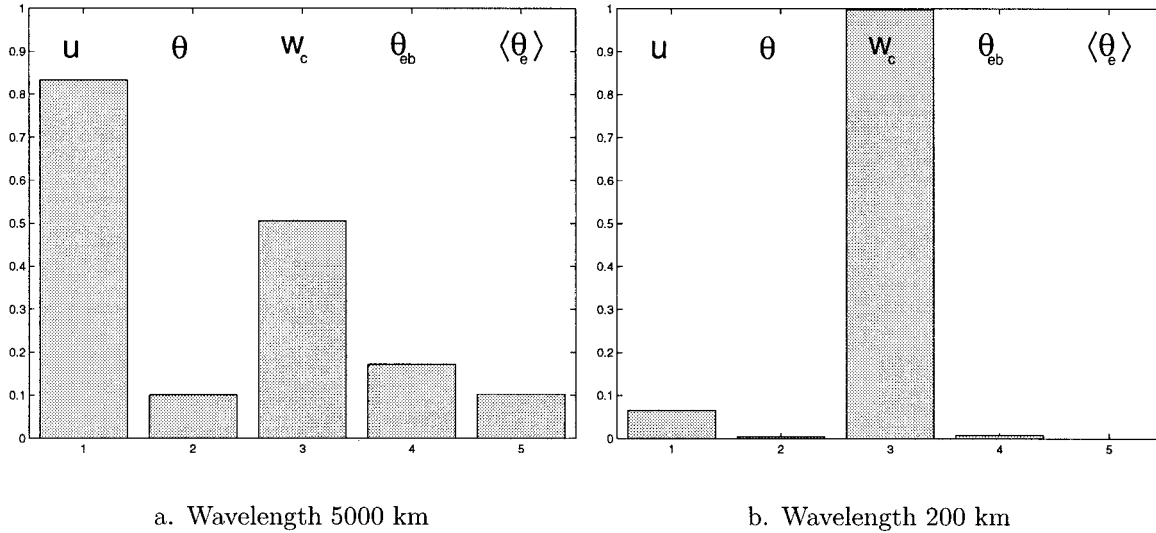


FIG. 4. Eigenvector structure of eastward moist gravity waves for the ICAPE system without rotation at wavelengths: 5000 km (a), and 200 km (b).

For example, in the regime involving the set of parameters from Table 1 completed with  $u_0 = 0.1 \text{ m s}^{-1}$  and  $\bar{u} = -0.1 \text{ m s}^{-1}$ , the superfast waves are unstable at the short wavelengths,  $L < 300 \text{ km}$ . This situation can be distinctly problematic for numerical models operating in the nonlinear regime, since the fast moving modes without physical significance can rapidly propagate and contaminate the solutions through nonlinear interactions. Therefore, it is desirable to design convective parameterizations that do not have superfast or other physically meaningless and potentially harmful modes.

The linearized analysis for the LPA scheme from YM<sup>2</sup> only examined special solutions involving the linearized moist gravity waves; the more detailed analysis of the complete set of all normal-mode solutions developed here reveals the existence of such nonphysical parasitic waves for the LPA scheme. The nonlinear numerical solutions with the LPA scheme presented in YM<sup>2</sup>E are extremely noisy. It is interesting to speculate that one nonphysical contribution to this noise involves the parasitic waves documented here. This is an interesting topic for future investigation.

### c. Waves in the ICAPE system

In the ICAPE system dynamic adjustment to CAPE fluctuations is replaced by instantaneous adjustment. Mathematically, the dimension of the linearized system and the number of normal modes in (3.3) are each reduced by one. Among the four normal modes in the ICAPE system, three can be identified as analogs of waves in the LPA system. Indeed, two of the modes are almost entirely equivalent to eastward and westward moist gravity waves, both in stability and wave properties, as illustrated in Fig. 3 for the eastward moist gravity waves. Figure 4 depicts the bar diagram for the

eigenvector structure of the moist gravity wave in the ICAPE system at sample wavelengths 5000 and 200 km. It is easy to see that the eigenvectors are virtually indistinguishable from those depicted for the LPA-generated moist gravity waves in Figs. 2c,d. The ICAPE-generated  $\langle\theta_e\rangle_c$  mode, not displayed here, is also entirely similar to its LPA-generated analog.

The remaining normal mode generated by the ICAPE scheme, however, has no counterpart in the LPA system. It is virtually a standing convective adjustment mode, with enormous damping rates at all wavenumbers,  $d(k) \approx -1000 \text{ day}^{-1}$ . At all wavenumbers, the eigenstructure of this mode has essentially all of its amplitude proportional to  $w_c$ ; thus, this mode represents rapid damping of CAPE perturbations. This single mode replaces the two parasitic superfast waves that are observed in the LPA scheme. The authors note that the superfast waves arise due to the presence of a large constant,

$$\frac{c_p \Gamma_m H}{W^2} \frac{\theta_{eb}^*}{\theta_0} = \begin{cases} 10\,000, & \text{for } \sigma_c = 0.01 \\ 400, & \text{for } \sigma_c = 0.002, \end{cases}$$

in the nondimensional version of the dynamic CAPE adjustment equation in (2.12) that sets a short timescale for spurious waves. In the ICAPE scheme this mechanism is shut off, which removes the unwanted superfast modes and replaces them with a superdamped standing wave, while keeping all physically relevant modes intact. The superdamped mode is associated with rapid adjustment to equilibrium of CAPE perturbations. This indicates that the ICAPE scheme has some features similar to CAPE adjustment schemes (Neelin and Yu 1994).

Moist gravity waves in the ICAPE system have stability properties that are almost entirely equivalent to those of moist gravity waves of the LPA system, as follows from the direct comparison of solid and long-

dashed curves in Fig. 3a. In particular, the maximum growth rate in both schemes is approximately equal to  $1.2 \text{ day}^{-1}$ . This rate corresponds to a moist gravity wave with wavelength 1000 km. The band of unstable waves for both schemes covers wavelengths in the range  $150 \text{ km} < L < 20\,000 \text{ km}$ . The maximum growth rate, the wavelength of the most unstable mode, and the range of instability all form useful diagnostics that will be utilized later in section 4c to address stability properties of the ICAPE system with rotation.

*d. Waves in ICAPE scheme without convective downdrafts and in the QE scheme*

An interesting question raised earlier in section 2c concerns the importance of small-scale convective downdrafts for the stability properties of convectively coupled models. This issue will be addressed within the simple framework of the ICAPE scheme, where convective downdrafts are switched off by setting  $\epsilon_p = 1$  in the equation for  $\theta_{eb}$  in (3.3). The dotted curve in Fig. 3a represents the growth rates associated with the ICAPE scheme without downdrafts. A comparison with the solid curve in Fig. 3a shows that instability is much more strongly pronounced without downdrafts, with the growth without bound at smaller wavelengths. This confirms the intuition that convective downdrafts tend to stabilize convectively coupled dynamics. In fact, the scheme without downdrafts is dominated by the effects of environmental convergence and, thus, effectively becomes a wave-conditional instability of the second kind (CISK) parameterization (Kuo 1974; Lindzen 1974; Emanuel 1994), where such catastrophic small-scale instabilities are prominent.

The generalized phase speeds for the ICAPE moist gravity waves without convective downdrafts are represented by the dotted curve in Fig. 3b. It is evident from this figure that at the largest planetary scales, the convective downdrafts have very little influence on the generalized phase speed. For scales shorter than 5000 km this situation changes dramatically. There, the absence of convective downdrafts slows down the waves significantly. For example, at a typical scale of 1000 km the generalized phase speeds of the ICAPE system with and without convective downdrafts are 12 and  $3 \text{ m s}^{-1}$ , correspondingly, while at a scale,  $L = 100 \text{ km}$ , the discrepancy is even stronger, with phase velocities of 11.5 and  $0.8 \text{ m s}^{-1}$ .

Next, a brief discussion is given for wave and stability properties of the scheme based on the QE assumption in (2.15). This model involves only three prognostic equations. A simple analysis shows that the three normal modes include eastward and westward moist gravity waves, extremely similar in their wave properties and eigenvector structure to moist gravity waves in the LPA and ICAPE systems, and the  $\langle \theta_e \rangle_z$  mode. The growth rates for eastward moist gravity waves are represented by the dot-dashed line in Fig. 3a. Deviations of the QE growth rates from the ICAPE and LPA growth rates at

large scales are relatively weak, while at small scales the picture changes qualitatively. Contrasting with the LPA and ICAPE schemes, where growth rates decrease with  $k$  and become negative at a finite wavelength, growth rates in the QE model quickly saturate with  $k$  at a positive value close to the maximum growth rate in the ICAPE model and remain at this value for all small scales.

A comparison of the solid and dot-dashed curves in Fig. 3b shows that the wave properties of QE moist gravity waves are remarkably similar to those of ICAPE waves; this is also true for the  $\langle \theta_e \rangle_z$  mode. Eigenvector structures of both QE-generated moist gravity waves and the  $\langle \theta_e \rangle_z$  mode are indistinguishable from their counterparts for the ICAPE-generated waves in an extremely wide range of scales, with at least  $50 \text{ km} < L < 40\,000 \text{ km}$ .

*e. Summary of properties for ICAPE, LPA, and QE schemes*

The results presented in the previous three sections demonstrate that ICAPE, LPA, and QE schemes present very similar wave and stability properties at large scales, as concerns physically relevant moist gravity waves and the  $\langle \theta_e \rangle_z$  mode. The behavior at small scales depends on the details of the particular convective parameterization. Of the three schemes, the authors argue that the ICAPE-based model, developed in section 2b, is preferable for numerical simulations in the fully nonlinear regime for the following reasons. The short-wave instability for moist gravity waves is suppressed in the ICAPE scheme, which is not true for the QE scheme, and the ICAPE scheme does not possess the parasitic nonphysical super-fast waves that are present in the LPA scheme. Therefore, the subsequent discussions will be focused on various additional properties for the model based on the ICAPE parameterization, with only occasional references to the other parameterizations.

#### 4. The effect of rotation on convectively coupled waves

The rotation of the earth plays an important role for atmospheric dynamics in the Tropics. It is well known (Gill 1982) that such widely observed phenomena as equatorially trapped Kelvin waves and Rossby and mixed Rossby-gravity waves owe their existence to the change in sign of the Coriolis parameter at the equator. However, it is a significantly more difficult task to study dynamics with rotation since an extra spatial dimension is required to resolve the meridional dependence. There is a wide spectrum of approaches used to model meridionally dependent equatorial dynamics, ranging from fully meridionally resolved models to approximations based on essentially no meridional dependence. An example of such an approximation is the model based on the so-called long-wave equatorial equations (Gill 1982; Heckley and Gill 1984; Neelin and Yu 1994). There,

for the standard dry shallow-water dynamics of the first baroclinic mode, the full set of equatorial Rossby and gravity waves is replaced by a reduced set of nondispersive modes in the limit of large zonal wavelength with meridional geostrophic balance. In such a model, all gravity waves and mixed Rossby–gravity waves are filtered.

In this section, the authors take an intermediate position between the two extremes that avoids full resolution but retains the most important structure in the meridional direction sufficient to break the east–west symmetry at large scales and to generate the most important effects of equatorial dynamics on the  $\beta$  plane. It is well known (Gill 1982) that the linearized system of dry shallow-water equations on the equatorial  $\beta$  plane can be represented through a sequence of decoupled wave systems by expanding the equations in the meridional direction in terms of parabolic cylinder functions. This decomposition reveals in an explicit form the Kelvin wave, the mixed Rossby–gravity wave, as well as a sequence of equatorial Rossby and gravity waves of various order in the meridional direction. The presence of parameterized convection and moist exchanges modifies the system; however, it is still possible to use a meridional expansion based on parabolic cylinder functions. The truncation procedure discussed in the next section reduces the full nonlinear system through projections on the first few meridional modes to a set of prognostic equations, each of which has no meridional dependence. As a result, the truncated system is significantly easier to analyze. At the same time, it will be shown to retain the most essential features of the rotationally driven dynamics for equatorially trapped modes, including slowly propagating moist gravity waves.

In their recent analysis of observational studies, Wheeler and Kiladis (1999) reported that gravity waves have a prominent signature in the spectral decomposition of propagating equatorial waves. In the dry dynamics, equatorial gravity waves are known to move with high phase speeds. For this reason, gravity waves are often ignored in the dry simulations. It has been pointed out in section 3 that convective coupling can significantly slow down gravity waves making them potentially important in the convectively coupled dynamics.

The truncated system proposed in this section has high zonal and crude meridional resolution. Such an approximation is unable to represent meridional motion at small scales, but is adequate for the description of waves propagating in the zonal direction, including moist gravity waves, even at the small scales. The truncation strategy proposed here provides a reasonable compromise between models that utilize numerically expensive high resolution in both zonal and meridional directions, but are unable to resolve the details of convection (e.g., Emanuel 1994) and schemes that sacrifice the meridional dependence for the high resolution of convective events, such as cloud-resolving models at the equator (Grabowski 1998).

### a. Meridional truncated equations and ICAPE linearization

Here, a reduced set of equations is derived based on truncation of the convectively coupled system in the meridional direction, and the subsequent linearization of these equations near the radiative–convective equilibrium. Formally, the truncation step precedes linearization and will be reported first. However, it can be shown that truncation and linearization can be performed in the reverse order, which is simpler for the actual computations.

For shallow-water dynamics on the equatorial  $\beta$  plane the following Riemann invariants (Gill 1982) are utilized,

$$q = \left( u - \frac{\bar{\alpha}\theta_{eb}^*}{V^2}\theta \right), \quad r = -\left( \frac{\bar{\alpha}\theta_{eb}^*}{V^2}\theta + u \right).$$

With these variables, the nondimensional equations for wind,  $\mathbf{u}$ , and dry potential temperature,  $\theta$ , can be rewritten in terms of the Riemann invariants,  $q$ ,  $r$ , and meridional velocity,  $v$ , as follows:

$$\begin{aligned} \frac{\partial q}{\partial t} &= -\frac{\partial q}{\partial x} - \left( \frac{\partial v}{\partial y} - yv \right) - \frac{1}{2} \left( \frac{T}{\tau_D} + \frac{T}{\tau_R} \right) q \\ &\quad + \frac{1}{2} \left( \frac{T}{\tau_D} - \frac{T}{\tau_R} \right) r - \frac{\bar{\alpha}T|Q_{R0}|}{V^2} w_c + N_1(\mathbf{U}), \\ \frac{\partial r}{\partial t} &= \frac{\partial r}{\partial x} - \left( \frac{\partial v}{\partial y} + yv \right) - \frac{1}{2} \left( \frac{T}{\tau_D} + \frac{T}{\tau_R} \right) r + \frac{1}{2} \left( \frac{T}{\tau_D} - \frac{T}{\tau_R} \right) q \\ &\quad - \frac{\bar{\alpha}T|Q_{R0}|}{V^2} w_c + N_2(\mathbf{U}), \\ \frac{\partial v}{\partial t} &= -\frac{1}{2} \left( \frac{\partial q}{\partial y} + yq \right) - \frac{1}{2} \left( \frac{\partial r}{\partial y} - yr \right) - \frac{T}{\tau_D} v + N_3(\mathbf{U}), \end{aligned} \quad (4.1)$$

where  $N_1(\mathbf{U})$ ,  $N_2(\mathbf{U})$ , and  $N_3(\mathbf{U})$  are the nonlinear advection and drag terms; and  $\mathbf{U} = (q, r, v, w_c, \theta_{eb}, \langle \theta_e \rangle_z)$  is the solution vector. The remaining equations are transformed in a similar way and are not reported here for brevity.

In the dry case, the linear part of (4.1) can be decomposed into a sequence of fully decoupled wave systems, based on expansion in terms of the parabolic cylinder functions,  $D_n$ :

$$\begin{aligned} \mathbf{U}(x, y, t) &= \sum_{n=0}^{\infty} \mathbf{U}_n(x, t) D_n(2^{1/2}y), \\ D_n(\xi) &= 2^{-n/2} F_n(2^{-1/2}\xi) \exp\left(-\frac{\xi^2}{4}\right), \\ F_n(\xi) &= (-1)^n \exp(\xi^2) \frac{d^n[\exp(-\xi^2)]}{d\xi^n}. \end{aligned} \quad (4.2)$$

Convective feedbacks to the linearized dry dynamics are explicitly represented by the terms with  $w_c$  in the first two equations in (4.1). These feedbacks generate nontrivial coupling among wave systems associated with different meridional numbers,  $n$ .

The purpose of the meridional truncation procedure is to retain the most observationally prominent waves and to discard the rest of the less important meridionally higher-order waves. For the simplest truncated system, only a few waves are retained that correspond to the four lowest meridional modes, with the following variables: 1)  $q_0$ , Kelvin wave; 2)  $q_1, v_0$ , mixed Rossby-gravity waves; 3)  $q_2, v_1, r_0$ , lowest-order Rossby and gravity waves, symmetric about the equator; and 4)  $q_3, v_2, r_1$ , lowest-order Rossby and gravity waves, antisymmetric about the equator. To obtain a closed set of convectively coupled equations, the lowest symmetric and antisymmetric components in the meridional expansion in (4.2) of the remaining variables,  $w_{c,0}, w_{c,1}, \theta_{eb,0}, \theta_{eb,1}, \langle \theta_e \rangle_{z,0}$ , and  $\langle \theta_e \rangle_{z,1}$ , are added to the set of large-scale variables above. To complete the truncation procedure, the moist coupling terms and nonlinear terms in each of the equations are projected onto the meridional mode that corresponds to a particular wave system. Since the parabolic cylinder functions form an orthonormal basis, the projection operator has the following simple form:

$$\begin{aligned} \text{Proj}_{D_n}(f(x, y, t)) &= (f(x, y, t), D_n(y)) \\ &= \int_{-\infty}^{\infty} f(x, y, t) D_n(y) dy. \end{aligned}$$

In the second step, the truncated equations are linearized near the radiative-convective equilibrium state. Also, the diagnostic relation in (2.13) based on the ICAPE assumption is utilized to eliminate  $w_c$  and to reduce the set of prognostic equations. After some algebra, the following linear system arises:

#### Symmetric modes

$$\begin{aligned} \frac{\partial q_0}{\partial t} + \frac{\partial q_0}{\partial x} &= -Q_1 q_0 + Q_2 r_0 - Q_3 \theta_{eb,0}, \\ \frac{\partial r_0}{\partial t} - \frac{\partial r_0}{\partial x} + 2^{1/2} v_1 &= -Q_1 r_0 + Q_2 q_0 - Q_3 \theta_{eb,0}, \\ \frac{\partial v_1}{\partial t} + 2^{1/2} q_2 - 2^{-1/2} r_0 &= -Q_4 v_1, \\ \frac{\partial q_2}{\partial t} + \frac{\partial q_2}{\partial x} - 2^{1/2} v_1 &= -Q_5 q_2, \\ \frac{\partial \theta_{eb,0}}{\partial t} &= Q_6 q_0 - Q_7 r_0 + Q_8 \frac{\partial}{\partial x} (q_0 - r_0) \\ &\quad - 2^{1/2} Q_8 v_1 - Q_9 \theta_{eb,0} \\ &\quad + Q_{10} \langle \theta_e \rangle_{z,0}, \\ \frac{\partial \langle \theta_e \rangle_{z,0}}{\partial t} &= Q_{11} q_0 - Q_{12} r_0 - Q_{13} \theta_{eb,0}. \end{aligned}$$

#### Antisymmetric modes

$$\begin{aligned} \frac{\partial q_1}{\partial t} + \frac{\partial q_1}{\partial x} - 2^{1/2} v_0 &= -Q_1 q_1 + Q_2 r_1 - Q_3 \theta_{eb,1}, \\ \frac{\partial v_0}{\partial t} + 2^{-1/2} q_1 &= -Q_4 v_0, \\ \frac{\partial r_1}{\partial t} - \frac{\partial r_1}{\partial x} + 2^{3/2} v_2 &= -Q_1 r_1 + Q_2 q_1 - Q_3 \theta_{eb,1}, \\ \frac{\partial v_2}{\partial t} + 3(2)^{-1/2} q_3 - 2^{-1/2} r_1 &= -Q_4 v_2, \\ \frac{\partial q_3}{\partial t} + \frac{\partial q_3}{\partial x} - 2^{1/2} v_2 &= -Q_5 q_3, \\ \frac{\partial \langle \theta_e \rangle_{z,1}}{\partial t} &= Q_{11} q_1 - Q_{12} r_1 - Q_{13} \theta_{eb,1}, \\ \frac{\partial \theta_{eb,1}}{\partial t} &= Q_6 q_1 - Q_7 r_1 + Q_8 \frac{\partial}{\partial x} (q_1 - r_1) \\ &\quad - 2^{3/2} Q_8 v_2 + 2^{1/2} Q_8 v_0 \\ &\quad - Q_9 \theta_{eb,1} + Q_{10} \langle \theta_e \rangle_{z,1}. \end{aligned} \quad (4.3)$$

The constants  $Q_1, \dots, Q_{13}$  depend on various physical parameters and are listed in the appendix. Remarkably enough, the variables that describe the modes symmetric in  $y$  (symmetric variables) are found only in the first six equations of the system in (4.3), while the antisymmetric variables are found only in the last seven equations. Therefore, the symmetric and antisymmetric parts of (4.3) decouple completely in the linearized system. This decoupling, of course, is destroyed in the fully nonlinear truncated system so these wave fields can interact through nonlinearity. The analysis of the linear system above utilizes eigenmodes in the form  $\mathbf{U}(x, t) = \mathbf{C} e^{i(kx - \omega(k)t) + d(k)t}$ , with the phase  $\omega(k)$  and normalized growth rate,  $d(k)$ , similar to section 3.

#### b. Classification of waves

The linear system in (4.3) describes the dynamics of dry variables coupled with moist exchanges of energy through convection, restricted to the first few meridional modes. Here, a discussion of wave properties of this system is given. The convectively coupled waves are also compared to the waves that arise in the dry system.

At large scales, errors introduced by truncation and convective parameterization have the least influence on the properties of the convectively coupled system. Therefore, a classification of moist waves will be based on the comparison of normal modes for (4.3) and the dry modes obtained by the same meridional truncation at the large scales (Gill 1982). Figure 5a presents the phases of the normal modes for (4.3), while Fig. 5b shows the phases of the corresponding dry waves, that is, dry Kelvin mode, dry mixed Rossby-gravity (MRG), and the lowest-order symmetric and antisymmetric dry Rossby and gravity

waves. The values of physical parameters in this example are taken from Table 1, with  $u_0 = 2 \text{ m s}^{-1}$ ,  $\bar{u} = -2 \text{ m s}^{-1}$ , and  $\sigma_c = 0.01$ . Remarkably enough, all dry equatorial waves have analogs in the system described by (4.3). This analogy is fully confirmed by the comparison of the underlying wave structures and flow patterns of moist and dry normal modes and provides quantitative support for the idea that the equatorial waves observed by Wheeler and Kiladis (1999) are moist convectively coupled waves. Based on this similarity, it is natural to extend the names of the dry modes to their moist counterparts and to introduce a moist Kelvin wave, a moist MRG wave, etc. The direct comparison of Figs. 5a and 5b shows that (generalized) phase velocities of the moist modes are slower than phase velocities of their dry counterparts. For example, at the wavelength  $L = 10\,000 \text{ km}$ , a moist Kelvin wave and a moist MRG propagate with phase velocities that are 65% and 55% slower than phase velocities of dry Kelvin and dry MRG waves. A similar deceleration is observed for symmetric and antisymmetric Rossby waves, as well as symmetric and antisymmetric westward gravity modes.

In addition to the moist modes that are classified according to their dry analogs, the  $13 \times 13$  system in (4.3) generates four more normal modes. All these extra modes are essentially standing waves that are represented by four nearly indistinguishable curves near  $\omega(k) = 0$  on the phase diagram in Fig. 5a. A more detailed analysis of growth rates and wave structure reveals that these modes are the symmetric and antisymmetric analogs of the  $\langle \theta_e \rangle_z$  mode and the superdamped convective adjustment mode discussed in section 3c. A simple check shows that the generalized phase speeds of the moist modes are fairly independent of the strength and direction of the mean flow, which means that the classification of moist waves given above can be extended for any mean flow.

At scales much shorter than the equatorial Rossby deformation radius, the effects of rotation are expected to play no significant role in the dynamics. Therefore, one expects that some of the normal modes with rotation become similar to the normal modes that arise in the absence of rotation, in the limit of large wavenumbers. This similarity is indeed observed and illustrated in Table 2. In the left column of this table various moist modes are listed, according to their large-scale classification given above. Apart from the moist Kelvin and moist MRG waves, all other modes include a symmetric and antisymmetric variety. In the right column the analogs of moist normal modes are reported based on comparisons at small scales. In particular, simple calculations show that the phase speed of the moist Kelvin and the eastward branch ( $k > 0$ ) of moist MRG wave decrease significantly with  $k$ , so that both modes become essentially equivalent to the eastward moist gravity wave generated by the system without rotation. Both symmetric and antisymmetric westward gravity waves converge at small scales to the moist westward gravity wave of the system without rotation. Interestingly

enough, symmetric and antisymmetric moist eastward gravity waves at small scales carry essentially no moisture and convection fluctuations, and both travel at the speed of a dry gravity wave,  $50 \text{ m s}^{-1}$ . The moist Rossby wave and the westward branch ( $k < 0$ ) of moist MRG waves become essentially standing waves at small scales and are dominated by meridional flow with very weak small-scale convection. Finally, both symmetric and antisymmetric  $\langle \theta_e \rangle_z$  modes and superdamped modes converge to their analogs from the system without rotation.

### c. Easterly mean wind and the transition to instability

Here the discussion is concentrated on the stability properties of normal modes for the system in (4.3) and the structure of unstable modes. Rotation breaks the east–west symmetry, and for simplicity only the system driven by easterly mean wind is considered here.

For compatibility with other parts of this paper, the standard set of parameters is adopted from Table 1, along with  $u_0 = 2 \text{ m s}^{-1}$ ,  $\sigma_c = 0.01$ , and an easterly mean flow of  $\bar{u} = -2 \text{ m s}^{-1}$ . Simple stability analysis reveals that an easterly mean wind triggers instability in the following eastward waves: 1) the moist Kelvin wave, and 2) the eastward branch of moist MRG wave. To estimate how the effects of rotation modify stability properties, the same stability diagnostics are utilized for these two modes as in the absence of rotation at the end of section 3c. The maximum growth rates remain almost unchanged by rotation, with 1.2 and  $1.1 \text{ day}^{-1}$  for the moist Kelvin and the eastward branch of moist MRG waves, as compared with  $1.2 \text{ day}^{-1}$  for the eastward gravity wave without rotation. The strongest instability tends to occur at slightly shorter wavelengths—compare approximately 800 and 550 km for the moist Kelvin and moist MRG waves to approximately 1000 km without rotation. The range of instability for the moist Kelvin waves includes the wavelengths  $125 \text{ km} < L < 40\,000 \text{ km}$  and is almost equivalent to the range of unstable modes without rotation, while the moist MRG waves are unstable in a slightly narrower range,  $150 \text{ km} < L < 10\,000 \text{ km}$ .

In Figs. 6 and 7 the actual flow patterns are presented that are associated with moist Kelvin and moist mixed Rossby–gravity waves, at the wavelength 700 km, near the peak of maximum growth for both waves. At this wavelength, moist Kelvin and moist MRG waves propagate with the generalized phase speeds of 12.1 and  $12.6 \text{ m s}^{-1}$ , which are significantly slower than 50 and  $50.6 \text{ m s}^{-1}$ , the phase speeds of dry Kelvin and dry MRG waves at this scale. Convective coupling introduces a weak meridional circulation to the flow pattern of the moist Kelvin wave. Strong zonal equatorial convergence at the bottom of the troposphere is augmented by weak meridional convergence, and it produces the ascending branch of a Walker-like circulation. The intensity of convective updrafts sets the spatial distribution of the strength of convective heating in this model, in accordance with the spatial structure of

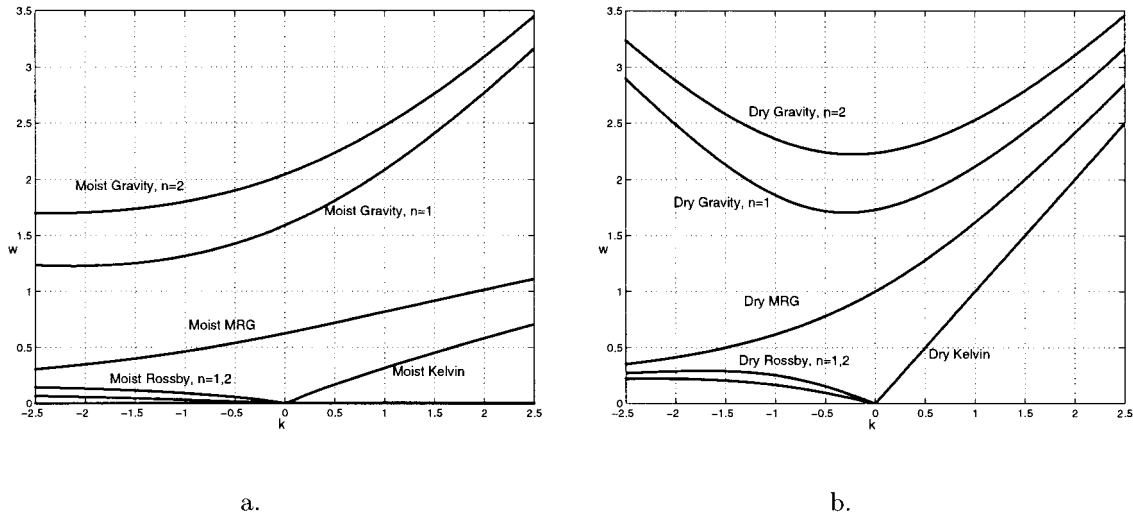


FIG. 5. Dispersion relation for equatorial Kelvin, mixed Rossby–gravity, and first two Rossby and gravity waves: (a) with convective coupling via the ICAPE scheme; (b) dry case, without convective coupling. Since the dispersion relation is skew symmetric, only the upper half-plane,  $\omega \geq 0$  is displayed.

the baroclinic heating mode. Figure 6 clearly indicates that regions of strong convective heating, represented by lighter shading, are positively correlated with the ascending branch of large-scale motion.

The flow pattern for the moist MRG wave presented in Fig. 7 is almost equivalent to its dry analog. Here, the regions of strong zonal convergence are located away from the equator and are accompanied by a weak meridional cross flow. Meridional circulation in this case is strong enough to generate a flow in the  $(y, z)$  plane similar to the Hadley cell pattern, clearly identifiable on the diagram. Positive convective heating is again in phase with the ascending branch of the vertical circulation associated with this wave.

Next, the transition to instability is studied here. The nonzero barotropic mean wind triggers the wind-induced surface heat exchange (WISHE) (Emanuel 1987; Yano and Emanuel 1991) mechanism that drives instabilities of the system in (4.3) through the forcing term,

$$\frac{C_o L}{h} \frac{(1 - \bar{\theta}_{eb}) \bar{u}}{(\bar{u}^2 + u_0^2)^{1/2}} u,$$

projected on the appropriate meridional components in the equations for  $\theta_{eb,0}$  and  $\theta_{eb,1}$  in (4.3). On the other hand, a simple check shows that in the absence of mean wind the WISHE mechanism is suppressed, and the linear system in (4.3) is stable. The mean wind in this model crudely represents the effects of midlatitude dynamics and, in general, does not have to be constant. Therefore, sensitivity to the strength of the mean wind can be utilized as a simplified model for studying the dependence of stability of the tropical wave system on the midlatitude dynamics.

The second important parameter that is intrinsically nonconstant and that significantly affects stability properties is the intensity of turbulent drag in the boundary

layer, parameterized by  $u_0$ , according to (2.11). The combined effect of barotropic mean wind and turbulent drag on stability is illustrated in Fig. 8. Here we show the boundaries separating stable and unstable regimes for moist Kelvin and moist MRG waves of the system in (4.3), in the parameter space of  $|\bar{u}|$  and  $u_0$ . The two curves are almost identical. The curve associated with the moist Kelvin wave is located just above the curve for the moist MRG wave, which corresponds to slightly stronger instability for the moist Kelvin wave. Also, transitions to instability for moist Kelvin waves (left branch of the curve) occur at slightly smaller values of  $|\bar{u}|$ , while reverse transitions to stability occur at larger values of  $|\bar{u}|$ . However, the moist MRG waves have nearly zero growth rates when the moist Kelvin waves become critical; thus, any transition to instability in the convectively coupled system involves both of these waves with the possibility of their nonlinear interaction. Table 3 lists various wave properties at criticality for both the Kelvin and moist MRG wave, for the values of  $u_0$  marked by diamonds and asterisks in Fig. 8. It is easy to see that both the phase and group velocities are fairly independent of the wavelength. Thus, both the moist Kelvin and moist MRG waves tend to propagate together in the transition to instability.

## 5. Concluding discussion

The structure of convectively coupled waves and instabilities has been analyzed in detail for three convective parameterizations, LPA, ICAPE, and QE, within the context of simplified shallow-water models. One of the novel features in these models is a turbulent drag parameterization [see Eq. (2.11)] that incorporates the nonzero effect of turbulence on the boundary layer even when the barotropic mean flow vanishes. This feature allows for a

TABLE 2. Classification of moist equatorial waves at large scales and behavior of moist equatorial waves at small scales.

Wave classification at large scales	Wave analog at small scales
Moist Kelvin wave	Eastward moist gravity wave (no rotation)
Moist eastward MRG wave	Eastward moist gravity wave (no rotation)
Symmetric and antisymmetric moist Rossby wave	Dry standing wave dominated by meridional flow
Moist westward MRG wave	Dry standing wave, meridional flow
Symmetric and antisymmetric eastward moist gravity wave	Dry eastward gravity wave
Symmetric and antisymmetric westward moist gravity wave	Westward moist gravity wave (no rotation)
Symmetric and antisymmetric superdamped mode	Superdamped mode (no rotation)
Symmetric and antisymmetric $\langle \theta_e \rangle_z$ mode	$\langle \theta_e \rangle_z$ mode (no rotation)

well-defined stable radiative–convective equilibrium when the mean flow vanishes and also facilitates the transition to instability studies reported in section 4c.

While the analysis presented here does not provide a definitive physical explanation for the wavelength of convectively coupled tropical waves, several important facts regarding the three model convective parameterizations are

established in section 3. This study establishes that introducing short finite-timescale processes involving the parametrization of small departures of CAPE through either LPA or ICAPE gives robust scale-selective behavior of moist gravity waves in contrast with strict QE. Unlike the QE parameterization, both the LPA and ICAPE schemes have scale-selective finite bands of unstable wavelengths centered around typical cluster and supercluster scales with virtually identical growth rates (see Fig. 3b) and wave structure (see Figs. 2c,d and 4) for the unstable waves. However, the LPA scheme also has the nonphysical superfast parasitic waves (see Figs. 1, 2a,b), which are undesirable for both physical and numerical purposes, while the new ICAPE parameterization removes the parasitic waves completely and replaces them by a single mode that strongly damps CAPE perturbations. While the LPA scheme has an attractive physical basis in attempting to incorporate shorter-timescale departures from strict quasi equilibrium, detailed analysis reveals the unexpected unattractive feature of superfast parasitic waves. Similar cautionary remarks apply in other attempts to model departure from quasi equilibrium in numerical general circulation models. For example, it would be interesting to see whether such superfast parasitic waves are present in other convective parameterizations, such as models with convective

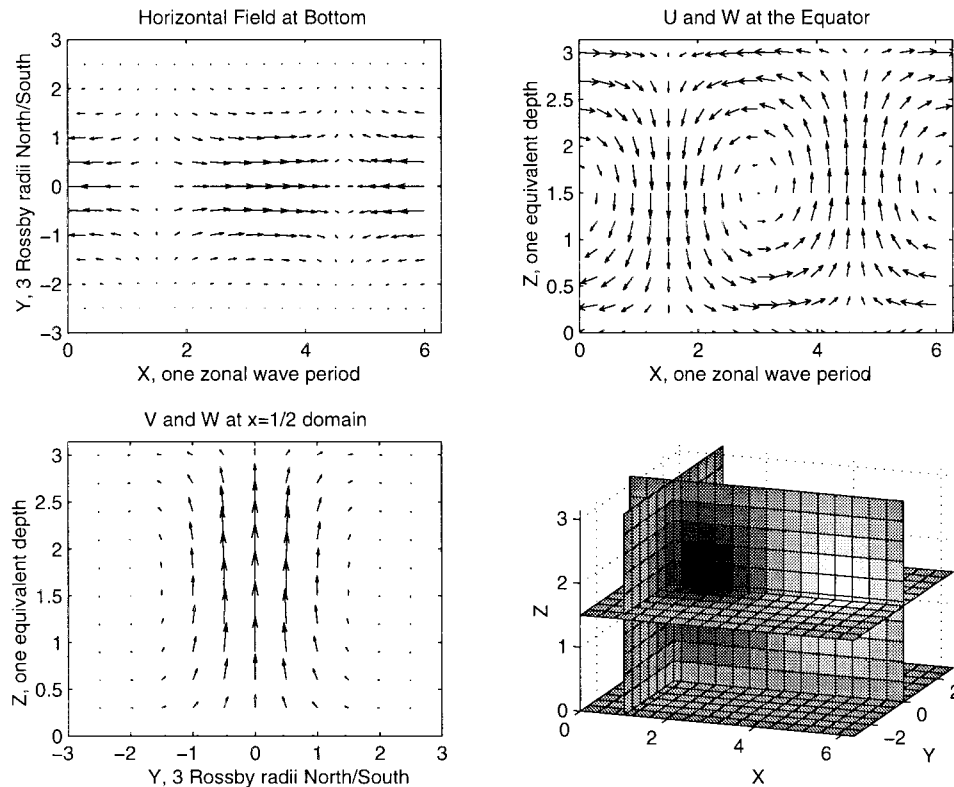


FIG. 6. Flow pattern associated with unstable moist Kelvin wave with the wavelength,  $L = 700$  km. From left to right and top to bottom: horizontal flow field at the bottom of the troposphere; flow in the zonal and vertical directions at the equator; flow in the meridional and vertical directions in the middle of one zonal wavelength; strength of convective heating, with light shading for positive heating, and dark shading for negative heating.

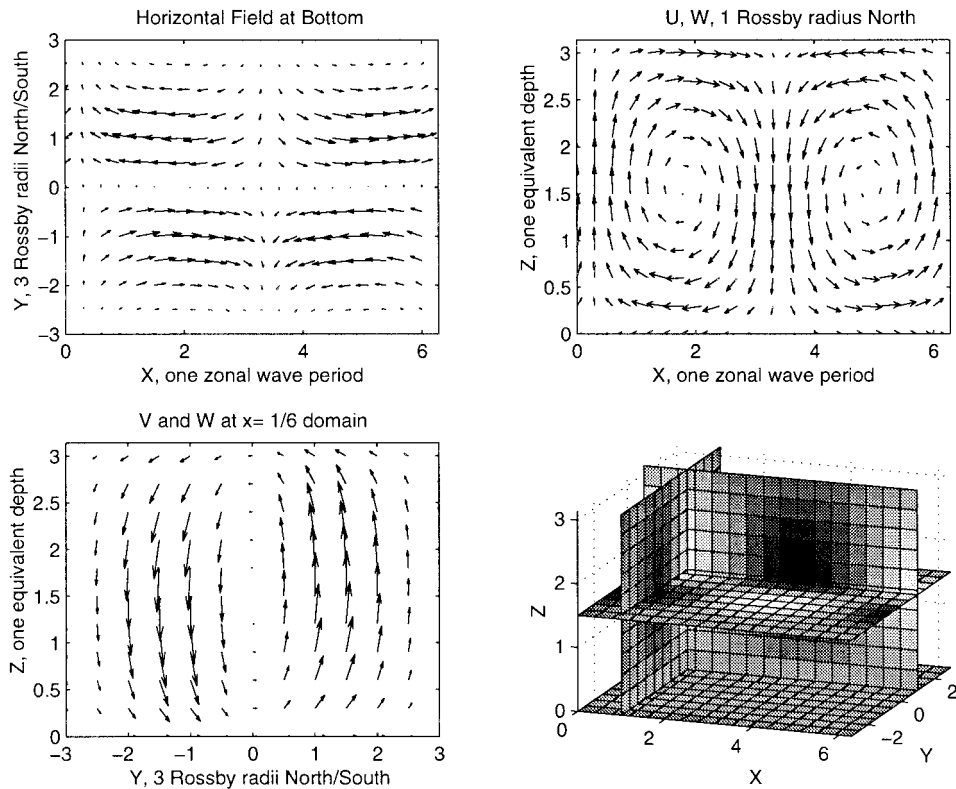


FIG. 7. Flow pattern associated with unstable moist eastward mixed Rossby-gravity wave with the wavelength  $L = 700$  km. From left to right and top to bottom: horizontal flow field at the bottom of the troposphere; flow in the zonal and vertical directions at one Rossby deformation radius north of the equator; flow in the meridional and vertical directions at  $1/6$  of one zonal wavelength; strength of convective heating, with light shading for positive heating, and dark shading for negative heating.

response time lag (Emanuel 1993). In section 3d, it is also established that if the effect of small-scale convective downdrafts on the boundary layer is suppressed, then the ICAPE scheme behaves like a standard wave-CISK parameterization with catastrophic instability for increasing wavenumbers (see Fig. 3a). Similar remarks are valid for the LPA parameterization.

An important topic studied here, in section 4c, is the fashion in which an imposed barotropic mean wind triggers a transition to instability in the Tropics through convectively coupled waves. This is the simplest analytical problem for studying the influence of midlatitudes on convectively coupled waves. For an easterly barotropic mean flow with the effect of rotation, both supercluster-scale moist Kelvin waves and cluster-scale mixed Rossby-gravity waves effectively participate in the transition to instability (see Fig. 8). Furthermore, both the instability band as well as the phase speed and group velocity of the critical waves in the transition to instability are remarkably insensitive to the detailed turbulent drag parameterization (see Table 3 above). A detailed weakly nonlinear theory for the transition to instability in these problems is being developed by the authors and will be presented elsewhere in the near future.

Finally, the results in section 4 for the ICAPE pa-

rameterization with the effects of rotation utilize a novel truncation procedure involving complete zonal resolution but low-order meridional truncation as presented in section 4a. As mentioned in section 4 this model is intermediate between equatorial long-wave approximations (Heckley and Gill 1984; Neelin and Yu 1994) and complete meridional resolution on the equatorial  $\beta$  plane. Such a strategy might be very useful in extending current equatorial cloud-resolving model simulations (Grabowski 1998; Grabowski et al. 2000) beyond purely two-dimensional flow in both a conceptually and computationally attractive framework. The authors together with W. Grabowski are developing this approach and will report on this in the near future.

*Acknowledgments.* The authors thank Mitch Moncrieff for his encouragement and scientific comments during the course of this work. Also, Jun-Ichi Yano provided a brief introduction to the papers YM<sup>2</sup>E and YM<sup>2</sup> during a visit to the Courant Institute. A. Majda is partially supported by Grants NSF DMS-9625795 and DMS-9972865, ONR N00014-96-1-0043, and ARO DAAG55-98-1-0129. M. Shefter is supported as a postdoctoral fellow by ONR N00014-96-1-0043 and NSF DMS-9625795 and DMS-9972865.

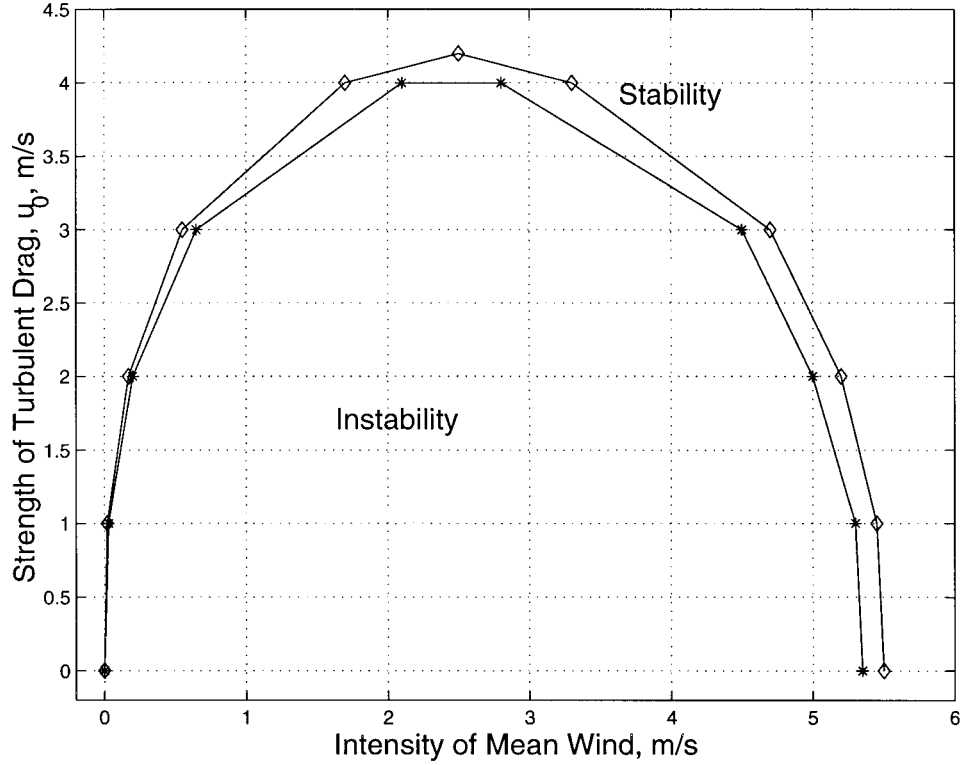


FIG. 8. Regions of linear stability and instability for the meridionally truncated ICAPE system forced by easterly barotropic mean flow. The parameter space includes the strength of barotropic mean flow,  $|\bar{u}|$ , and the strength of turbulent drag, expressed via mean velocity fluctuations,  $u_0$ . The top and bottom curves represent the critical values of mean wind required to generated instability of moist Kelvin (diamonds) and moist mixed Rossby–gravity (asterisks) waves, for various values of  $u_0$ .

## APPENDIX

### Constants Used in Eq. (4.3)

The constants  $Q_1, \dots, Q_{13}$  are computed according to the following formulas:

TABLE 3. Transition to instability for the moist Kelvin wave and the eastward branch of mixed Rossby–gravity waves driven by easterly barotropic mean wind in the meridionally truncated ICAPE system.

Drag, m s <sup>-1</sup>	Critical wind, m s <sup>-1</sup>	Wavelength, km	Phase speed, m s <sup>-1</sup>	Group speed, m s <sup>-1</sup>
Moist Kelvin wave				
1	-0.02	1600	12.1	11.6
2	-0.17	1350	12.1	12.0
3	-0.55	1250	12.0	11.7
4	-1.7	1000	12.0	11.8
4.2	-2.5	900	12.0	11.8
Moist mixed Rossby–gravity wave, eastward branch				
1	-0.03	1000	12.9	11.0
2	-0.20	800	12.6	11.3
3	-0.65	725	12.5	11.4
4	-2.1	675	12.4	11.5

$$Q_1 = \frac{1}{2}(M_1 + M_2 + M_4 + \gamma M_5),$$

$$Q_2 = \frac{1}{2}(M_1 + M_2 - M_4 - \gamma M_5), \quad Q_3 = \alpha' M_5,$$

$$Q_4 = M_2 + M_3, \quad Q_5 = \frac{1}{2}(M_1 + M_2 + M_4),$$

$$Q_6 = \frac{1}{2}\left(M_6 - \frac{\gamma M_8}{\alpha'}\right), \quad Q_7 = \frac{1}{2}\left(M_6 + \frac{\gamma M_8}{\alpha'}\right),$$

$$Q_8 = \frac{H_m}{2h} \left[ \bar{\theta}_{eb} \left( 1 + \frac{h}{H} \right) - \langle \bar{\theta}_e \rangle_z \right],$$

$$Q_9 = M_7 + M_8 + M_9, \quad Q_{10} = \frac{TW\sigma_c}{h\epsilon_p},$$

$$Q_{11} = \frac{1}{2}\left(M_{10} + \frac{M_4}{\alpha'}\right), \quad Q_{12} = \frac{1}{2}\left(M_{10} - \frac{M_4}{\alpha'}\right),$$

$$Q_{13} = \frac{C_0 L}{H} (\bar{u}^2 + u_0^2)^{1/2}, \quad (\text{A.1})$$

with

$$\begin{aligned}
M_1 &= \frac{C_D L}{h} \frac{2\bar{u}^2 + u_0^2}{(\bar{u}^2 + u_0^2)^{1/2}}, & M_2 &= \frac{T}{\tau_D}, \\
M_3 &= \frac{C_D L}{h} (\bar{u}^2 + u_0^2)^{1/2}, & M_4 &= \frac{T}{\tau_R}, \\
M_5 &= \frac{T |Q_{RO}| c_p \Gamma_m H \theta_{eb}^*}{\theta_{eb}^* W^2 \theta_0}, \\
M_6 &= \frac{C_\theta L}{h} (1 - \bar{\theta}_{eb}) \frac{\bar{u}}{(\bar{u}^2 + u_0^2)^{1/2}}, \\
M_7 &= \frac{C_\theta L}{h} (\bar{u}^2 + u_0^2)^{1/2}, \\
M_8 &= \frac{TW\sigma_c}{h\epsilon_p} \left[ \bar{\theta}_{eb} \left( 1 + \frac{h}{H} \right) - \langle \bar{\theta}_e \rangle_z \right] \frac{c_p \Gamma_m H \theta_{eb}^*}{W^2 \theta_0}, \\
M_9 &= \frac{TW\sigma_c}{h\epsilon_p} \left( 1 + \frac{h}{H} \right), \\
M_{10} &= \frac{C_\theta L}{H} (1 - \bar{\theta}_{eb}) \frac{\bar{u}}{(\bar{u}^2 + u_0^2)^{1/2}}, & \alpha' &= \frac{\bar{\alpha} \theta_{eb}^*}{V^2}. \quad (\text{A.2})
\end{aligned}$$

## REFERENCES

- Arakawa, A., and W. H. Schubert, 1974: Interaction of a cumulus cloud ensemble with the large-scale environment, Part I. *J. Atmos. Sci.*, **31**, 674–701.
- Chao, W. C., and S. Lin, 1994: Tropical intraseasonal oscillation, super cloud clusters, and cumulus convection schemes. *J. Atmos. Sci.*, **51**, 1282–1297.
- , and L. Deng, 1998: Tropical intraseasonal oscillation, super cloud clusters, and cumulus convective schemes. Part II: 3D aquaplanet simulations. *J. Atmos. Sci.*, **55**, 690–709.
- Emanuel, K. A., 1987: An air–sea interaction model of intraseasonal oscillations in the tropics. *J. Atmos. Sci.*, **44**, 2324–2340.
- , 1993: The effect of convective response time on WISHE models. *J. Atmos. Sci.*, **50**, 1763–1775.
- , 1994: *Atmospheric Convection*. Oxford Press, 427 pp.
- , J. D. Neelin, and C. S. Bretherton, 1994: On large-scale circulations in convecting atmosphere. *Quart. J. Roy. Meteor. Soc.*, **120**, 1111–1143.
- Gill, A. E., 1982: *Atmosphere–Ocean Dynamics*. Academic Press, 662 pp.
- Goswami, P., and B. N. Goswami, 1991: Modification of  $n = 0$  equatorial waves due to interaction between convection and dynamics. *J. Atmos. Sci.*, **48**, 2231–2244.
- Grabowski, W. W., 1998: Toward cloud resolving modeling of large-scale tropical circulations: A simple cloud microphysics parameterization. *J. Atmos. Sci.*, **55**, 3283–3298.
- , J.-I. Yano, and M. W. Moncrieff, 2000: Cloud resolving modeling of tropical circulations driven by large-scale SST gradients. *J. Atmos. Sci.*, **57**, 2022–2039.
- Heckley, W. A., and A. E. Gill, 1984: Some simple analytical solutions to the problem of forced equatorial long waves. *Quart. J. Roy. Meteor. Soc.*, **110**, 203–217.
- Kuo, H. L., 1974: Further studies of the influence of cumulus convection on large-scale flow. *J. Atmos. Sci.*, **31**, 1232–1240.
- Lin, J. W.-B., J. D. Neelin, and N. Zeng, 2000: Maintenance of tropical intraseasonal variability: Impact of evaporation–wind feedback and midlatitude storms. *J. Atmos. Sci.*, **57**, 2793–2823.
- Lindzen, R. S., 1974: Wave-CISK in the tropics. *J. Atmos. Sci.*, **31**, 156–179.
- Madden, R. A., and P. R. Julian, 1972: Description of global-scale circulation cells in the tropics with a 40–50 day period. *J. Atmos. Sci.*, **29**, 1109–1123.
- , and —, 1994: Observations of the 40–50-day tropical oscillation—A review. *Mon. Wea. Rev.*, **122**, 814–837.
- Nakazawa, T., 1988: Tropical super cluster within intraseasonal variations over the western Pacific. *J. Meteor. Soc. Japan*, **66**, 823–839.
- Neelin, J. D., and J. Yu, 1994: Modes of tropical variability under convective adjustment and the Madden–Julian oscillation. Part I: Analytical theory. *J. Atmos. Sci.*, **51**, 1876–1894.
- , and N. Zeng, 1999: The first quasi-equilibrium tropical circulation model—Formulation. *J. Atmos. Sci.*, submitted.
- , I. M. Held, and K. H. Cook, 1987: Evaporation–wind feedback and low-frequency variability in the tropical atmosphere. *J. Atmos. Sci.*, **44**, 2341–2348.
- Wheeler, M., and G. N. Kiladis, 1999: Convectively coupled equatorial waves: Analysis of clouds and temperature in the wave-number–frequency domain. *J. Atmos. Sci.*, **56**, 374–399.
- Yano, J.-I., and K. A. Emanuel, 1991: An improved model of the equatorial troposphere and its coupling to the stratosphere. *J. Atmos. Sci.*, **48**, 377–389.
- , J. C. McWilliams, M. W. Moncrieff, and K. A. Emanuel, 1995: Hierarchical tropical cloud systems in an analog shallow-water model. *J. Atmos. Sci.*, **52**, 1723–1742.
- , M. W. Moncrieff, and J. C. McWilliams, 1998: Linear stability and single-column analyses of several cumulus parameterization categories in a shallow-water model. *Quart. J. Roy. Meteor. Soc.*, **124**, 983–1005.
- Zeng, N., and J. D. Neelin, 1999: A land–atmosphere interaction theory for the tropical deforestation problem. *J. Climate*, **12**, 857–872.